# Impaired viral infection and reduced mortality of diatoms in iron-limited oceanic regions

Chana F. Kranzler[1]✉, Mark A. Brzezinski[2], Natalie R. Cohen[3,4], Robert H. Lampe[3,5], Michael Maniscalco[2], Claire P. Till[6,7], James Mack[1], Jason R. Latham[1], Kenneth W. Bruland[6], Benjamin S. Twining[8], Adrian Marchetti[3] and Kimberlee Thamatrakoln[1]✉

**Diatom primary productivity is tightly coupled with carbon export through the ballasted nature of the silica-based cell wall, linking the oceanic silicon and carbon cycles. However, despite low productivity, iron (Fe)-limited regimes are considered 'hot spots' of diatom silica burial with enhanced carbon export efficiency, raising questions about the mechanisms driving the biogeochemistry of these regions. Marine viruses are classically recognized as catalysts of remineralization through host lysis, short-circuiting the trophic transfer of carbon and facilitating the retention of dissolved organic matter and associated elements in the surface ocean. Here we used metatranscriptomic analysis of diatoms and associated viruses, along with a suite of physiological and geochemical metrics, to study the interaction between diatoms and viruses in Fe-limited regimes of the northeast Pacific. We found low cell-associated diatom virus diversity and abundance in a chronically Fe-limited region of the subarctic northeast Pacific. In a coastal upwelling region of the California Current, transient iron limitation also substantially reduced viral replication. These observations were recapitulated in Fe-limited cultures of the bloom-forming, centric diatom, *Chaetoceros tenuissimus*, which exhibited delayed virus-mediated mortality in addition to reduced viral replication. We suggest Fe-limited diatoms escape viral lysis and subsequent remineralization in the surface ocean, providing an additional mechanism contributing to enhanced carbon export efficiency and silica burial in Fe-limited oceanic regimes.**

Diatoms contribute up to 40% of marine primary production[1] and have silicified cell walls that ballast substantial vertical flux of particulate organic matter out of the surface into the deep ocean[2]. In high-nutrient, low-chlorophyll regions of the open ocean and along some coastal upwelling margins, iron (Fe) availability limits diatom production[3–5] and may contribute to the decoupling of primary productivity and export efficiency in these waters[6–8]. Fe-limited waters are biogeochemically distinct, characterized by enhanced drawdown of silicic acid relative to nitrate by Fe-limited diatoms, which leads to high cellular silicon (Si):nitrogen (N) and Si:carbon (C)[9,10]. These regions can also exhibit elevated diatom carbon export efficiency[6–8] and markedly high burial of biogenic silica ($bSiO_2$) relative to organic carbon in underlying sediments[11]. These 'hot spots' of silica burial contribute to widespread limitation of diatom silica production rates in the surface ocean, linking the Fe, Si and C cycles, and may impose a global constraint on the drawdown of atmospheric $CO_2$ and export production[12–14]. Together, these observations underscore the importance of elucidating the underlying chemical, physical and biological interactions that dictate the fate of diatom organic matter and associated elements in the ocean.

Viral infection of microbes is a major conduit for elemental cycling in the ocean, transforming the biogeochemical flux of nutrients and carbon, and toggling the balance between export and remineralization processes[15,16]. By fuelling the microbial loop with dissolved organic matter released during host lysis, viruses circumvent the transfer of particulate organic matter to depth or higher trophic levels through the 'viral shunt'[17]. We recently reported accelerated virus-mediated mortality in Si-limited diatoms, demonstrating a role for nutrient availability in facilitating the viral shunt[18]. However viral infection can also 'shuttle' organic matter out of the surface ocean by stimulating processes that facilitate export such as particle aggregation[19,20] and spore formation[21], highlighting the dynamic, biogeochemical consequences of host–virus interactions. Here we explored diatom host–virus dynamics in Fe-limited regimes of the northeast Pacific Ocean.

## Biogeochemically distinct phytoplankton assemblages

Our study encompassed five biogeochemically distinct sites in the iron mosaic of the California upwelling zone[9] (CUZ) and along a natural Fe gradient (Line P) in the subarctic northeast Pacific Ocean (Fig. 1a). Iron supply to the CUZ (sites S1, S2 and S4), delivered via riverine inputs and sediment resuspension of the continental shelf, is constrained primarily by shelf width along this boundary, generating a mosaic of steep along-shore gradients in bioavailable Fe[22]. In contrast, Fe is largely supplied along Line P (sites P4 and P26 or Ocean Station Papa[23]) through atmospheric deposition and horizontal advection with bioavailable Fe decreasing from near to offshore, resulting in a classical Fe-limited, high-nutrient, low-chlorophyll region (Fig. 1a). Among these sites, $bSiO_2$ concentrations ranged from 0.27 to 12.9 μM and chlorophyll *a* (chl *a*) concentrations (>5 μm) ranged from 0.08 to 12.3 μg $l^{-1}$, with the

[1]Department of Marine and Coastal Sciences, Rutgers University, New Brunswick, NJ, USA. [2]Marine Science Institute and the Department of Ecology Evolution and Marine Biology, University of California, Santa Barbara, CA, USA. [3]Department of Marine Sciences, University of North Carolina, Chapel Hill, NC, USA. [4]Marine Chemistry & Geochemistry, Woods Hole Oceanographic Institution, Woods Hole, MA, USA. [5]Integrative Oceanography Division, Scripps Institution of Oceanography, University of California, San Diego, La Jolla, CA, USA. [6]Department of Ocean Sciences, University of California, Santa Cruz, CA, USA. [7]Chemistry Department, Humboldt State University, Arcata, CA, USA. [8]Bigelow Laboratory for Ocean Sciences, East Boothbay, Maine, ME, USA. ✉e-mail: chana.kranzler@marine.rutgers.edu; thamat@marine.rutgers.edu

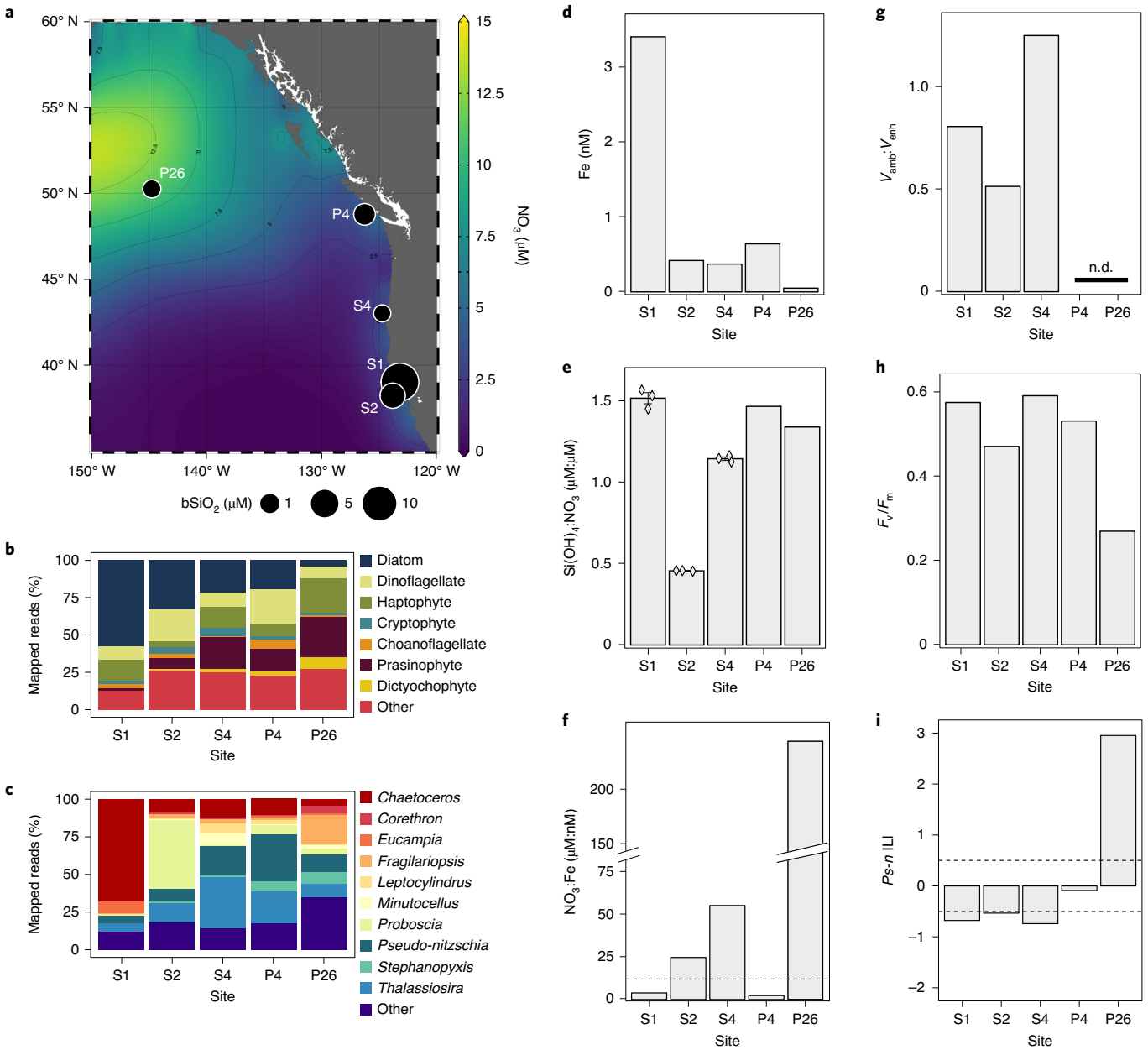


**Fig. 1 | Biogeochemical, physiological and molecular characteristics of initial phytoplankton communities in the northeast Pacific. a**, Mean surface nitrate concentration and sites (circles); symbol size depicts biogenic silica concentration. **b**,**c**, Relative transcript abundance of the major eukaryotic phytoplankton taxa (**b**) and diatom genera (**c**). **d**, Dissolved Fe concentrations. **e**, $Si(OH)_4$:$NO_3$ (mean ± standard error; diamonds represent individual measurements, $n = 3$). **f**, $NO_3$:Fe; dashed line denotes potential Fe limitation (12 μmol:nmol)[27]. **g**, Si stress ($V_{amb}$:$V_{enh}$); ~1 indicates no stress. n.d. indicates no data. **h**, Photosynthetic efficiency ($F_v/F_m$). **i**, *Ps-n* ILI[24]; values >0.5 and <−0.5 (dashed lines) indicate Fe-limited and Fe-replete growth, respectively.

lowest biomass by both metrics at S4 and P26, and the highest at S1 (Fig. 1a and Extended Data Table 1). Taxonomic distribution of mapped reads using metatranscriptomic assemblies confirmed diatoms were transcriptionally active at all sites, accounting for 4–57% of the total reads, with the highest proportion at S1 and the lowest at P26 (Fig. 1b and Supplementary Data 1). Within diatoms, *Chaetoceros*, *Pseudo-nitzschia* and *Thalassiosira* genera accounted for 25–78% of the transcripts at all sites, with notable representation of *Proboscia* at S2 (46%) and *Fragilariopsis* at P26 (19%; Fig. 1c and Supplementary Data 1).

A suite of biogeochemical, physiological and molecular diagnostics were used to determine the initial nutrient regime at each site[24–26] (Fig. 1d–i and Extended Data Table 1). In the CUZ, the site with the highest biomass, S1, was characterized by ≥13.7 μM nitrate and silicic acid (Extended Data Table 1), the highest dissolved Fe (3.39 nM; Fig. 1d), $Si(OH)_4$:$NO_3$ > 1 (Fig. 1e) and a $NO_3$:Fe ratio below the threshold for anticipated Fe limitation[27] (Fig. 1f). All metrics suggest a nutrient-replete regime at S1. Consistent with these observations, kinetic limitation of Si uptake (that is, Si stress; $V_{ambient}$:$V_{enhanced}$ [$V_{amb}$:$V_{enh}$]; Fig. 1g), photosynthetic efficiency (variable fluorescence [$F_v$]:maximum fluorescence [$F_m$]; $F_v/F_m$; Fig. 1h) and the iron limitation index for *Pseudo-nitzschia*[24] (*Ps-n* ILI; Fig. 1i) did not show any physiological or molecular signatures of nutrient limitation at S1. Despite its geographic proximity to S1, S2 had

substantially lower biomass and dissolved Fe (0.42 nM) and was depleted in silicic acid relative to nitrate (Fig. 1a,d–e; and Extended Data Table 1). Furthermore, the diatom assemblage exhibited a Si stress value of 0.51, indicating substantial substrate limitation of Si uptake (Fig. 1g). Although $F_v/F_m$ and *Ps-n* ILI at S2 were not consistent with Fe limitation at the time of sampling (Fig. 1h–i), elevated $NO_3$:Fe suggested the potential for impending Fe limitation with further nutrient consumption (Fig. 1f). Site S4 was characterized by high nitrate and silicic acid (≥16.9 µM), 0.31 nM dissolved Fe and the lowest initial biomass (Fig. 1a,d and Extended Data Table 1). Similar to S2, $F_v/F_m$ and *Ps-n* ILI did not indicate Fe limitation at S4 (Fig. 1h,i), but elevated $NO_3$:Fe suggested the potential for iron limitation (Fig. 1f). No signs of Si limitation were apparent at S4 with $Si(OH)_4$:$NO_3 \approx 1$ and a Si stress value of 1.25 (Fig. 1e,g).

Along Line P, biomass ($bSiO_2$ and chl *a*) was higher nearshore at site P4, with silicic acid and nitrate ≤2.2 µM, 0.64 nM dissolved Fe (Fig. 1a,d and Extended Data Table 1) and depletion of nitrate relative to silicic acid ($Si(OH)_4$:$NO_3 > 1$; Fig. 1e), suggesting nitrate limitation at the time of sampling. The $NO_3$:Fe ratio, $F_v/F_m$ and *Ps-n* ILI at P4 did not indicate iron limitation (Fig. 1f,h–i). In contrast, the assemblage at P26 displayed strong signs of Fe limitation including low biomass, silicic acid and nitrate both ≥11.7 µM, and 0.05 nM dissolved Fe (Fig. 1a,d and Extended Data Table 1). These observations were further supported by a greatly elevated $NO_3$:Fe ratio, impaired photosynthetic efficiency and a *Ps-n* ILI above the threshold for Fe-limited growth[24] (Fig. 1f,h–i), consistent with its classification as a chronically Fe-limited regime[28].

At each site, shipboard incubations were performed with added iron (+Fe) or desferrioxamine B (DFB; Extended Data Fig. 1), a strong Fe-binding ligand used to rapidly induce Fe limitation, alongside an unamended control (Ctrl). Together, these treatments enabled the characterization of the physiological and molecular response to fluctuating iron supply as previously reported[24–26], and provided further support for the initial underlying nutrient regime at each site. At S1, there was no measurable response in biomass or $F_v/F_m$ to +Fe[25,26] (Extended Data Fig. 1), further establishing its status as nutrient replete. The assemblage at S2 also did not respond to +Fe (Extended Data Fig. 1), but Si stress increased in severity by the first timepoint ($t_{48}$), even after an initial spike of Si to this incubation (see Methods), dropping from 0.51 to 0.16 ± 0.03 (Extended Data Fig. 2) and further confirming Si limitation across all treatments. At S4, the assemblage displayed a positive growth response to +Fe relative to the Ctrl (Extended Data Fig. 1), suggesting the onset of iron limitation in this recently upwelled community[25,26,29]. Along Line P, the P4 assemblage exhibited no growth response to +Fe; in contrast, both chl *a* concentration and $F_v/F_m$ sharply increased at P26 in response to +Fe, supporting severe Fe limitation at this site. Together, these sites encompassed diverse nutrient regimes, ranging from nutrient replete (S1) to limited for silicon (S2), nitrate (P4) and iron (P26; Extended Data Table 1).

## Divergent signatures of infection across nutrient regimes

To explore the prevalence of viral infection across these ecophysiologically distinct diatom communities, we used metatranscriptomic analysis of size-fractionated biomass to simultaneously detect both host (diatom) and cell-associated viral transcripts, the latter used as a proxy for viral infection. Diatom virus contigs were identified using a homology-based query with the taxonomic gene markers replicase (Rep) and RNA-dependent RNA polymerase (RdRp) from known single-stranded (ss) DNA- and ssRNA-containing diatom viruses, respectively. No sequences with homology to ssDNA diatom viruses were recovered. In contrast, we identified 144 unique cell-associated ssRNA diatom virus-like contigs (Supplementary Data 3; Expect (*E*) value $< 10^{-3}$). Phylogenetic placement within *Picornavirales* indicated that 79 of these contigs grouped among known diatom viruses (Extended Data Fig. 3) and were selected for further analysis. Selected contigs had a median length of 392 bp, but ranged from 124 to 8,999 bp, indicating the recovery of several near-complete viral genomes (~9 kb in length; Extended Data Fig. 3). Viral contig reads were normalized to total diatom transcripts to enable comparison across samples with different diatom biomass[18] and assess the contribution of individual and total virus contigs in the initial sample ($t_0$) and throughout each incubation. Although a subset of diatom virus contigs were shared across samples, hierarchical clustering of contig abundance revealed unique distribution patterns at each site (Fig. 2a). Diatom viruses were strikingly sparse in the Fe-limited P26 assemblage, with only three virus contigs identified, low viral diversity and low total cell-associated diatom virus abundance (Fig. 2). S1 and S2 had the highest number of distinct virus contigs (44 and 39 of the 79, respectively; Fig. 2a), with four dominant, highly abundant contigs at S2. Among all sites, S2 had ~1,000-fold higher total cell-associated diatom virus abundance (Fig. 2c), and was the only site in which a majority (56–75%) of viral contigs present at $t_0$ increased in abundance across all treatments (Extended Data Fig. 4). Furthermore, 13 additional virus contigs appeared at $t_{48}$, while only three virus contigs disappeared from at least one treatment (Extended Data Fig. 5). These data illustrate an actively progressing viral infection in the severely Si-stressed assemblage at S2, notably consistent with our previous findings that Si limitation facilitates virus infection in diatoms[18].

The low diatom virus diversity and abundance at P26, taken together with diagnostic signatures of severe Fe limitation (Fig. 1 and Extended Data Fig. 1), raised the possibility of a relationship between Fe availability and viral infection in diatoms. The actively infected diatom community at S2 allowed us to test the hypothesis that Fe limitation impairs virus replication in the manipulative shipboard incubations. Differential expression analysis of diatom transcripts at $t_{48}$ identified 105, 471 and 1,407 contigs in the DFB/Ctrl, Ctrl/+Fe and DFB/+Fe comparisons, respectively (Fig. 3 and Supplementary Data 4). No striking differences in iron homeostasis-related transcripts were observed between Ctrl and DFB treatments (Fig. 3a). However, when compared with +Fe, both Ctrl and DFB treatments exhibited clear overrepresentation of established Fe-limitation-responsive genes, including Fe-starvation-induced proteins (*ISIPs*) and plastocyanin (*petE*), as well as a suite of antioxidant genes such as peroxiredoxin (*prx*) and thioredoxin-dependant peroxidase (*tpx*; Fig. 3b,c). In addition, haem oxygenase (*HMOX*), widely recognized for its cytoprotective response to oxidative stress[30], with a potential role in repartitioning cellular Fe[31], was among the most highly upregulated transcripts (798-fold, false discovery rate (FDR) = $1.00 \times 10^{-9}$ for DFB/+Fe; 891-fold, FDR = $7.43 \times 10^{-10}$ for Ctrl/+Fe), consistent with lab studies of Fe-limited diatoms[32,33]. In the +Fe treatment, contigs involved in Fe-dependent photosynthetic electron transport and nitrogen assimilation were overrepresented, in line with previous studies[25,34], suggesting that the addition of Fe prevented the onset of Fe limitation (Fig. 3b,c). These transcriptional patterns demonstrate unequivocal Fe limitation in both Ctrl and DFB treatments at $t_{48}$ of the S2 incubation, concurrent with Si limitation (Extended Data Fig. 2).

Interestingly, the molecular delineation between Fe-replete (+Fe) and Fe-limited (Ctrl and DFB) conditions at S2 could also be extended to cell-associated diatom virus contig abundance. Overall, the aforementioned increase in diatom virus contig abundance from $t_0$ to $t_{48}$ was more pronounced in the +Fe treatment (median fold change of ~3 and ~2 in Fe-replete and Fe-limited treatments, respectively; Extended Data Fig. 5). In pairwise comparisons at $t_{48}$, 55% of viral contigs did not differ in abundance between Fe-limited treatments, compared with 30% of contigs between +Fe and Ctrl or DFB treatments (Fig. 3d–f). Of the 70% of viral contigs that exhibited a ≥2-fold change in the +Fe treatment, 86% and 78% increased in the +Fe/Ctrl and +Fe/DFB comparisons, respectively (Fig. 3e,f),

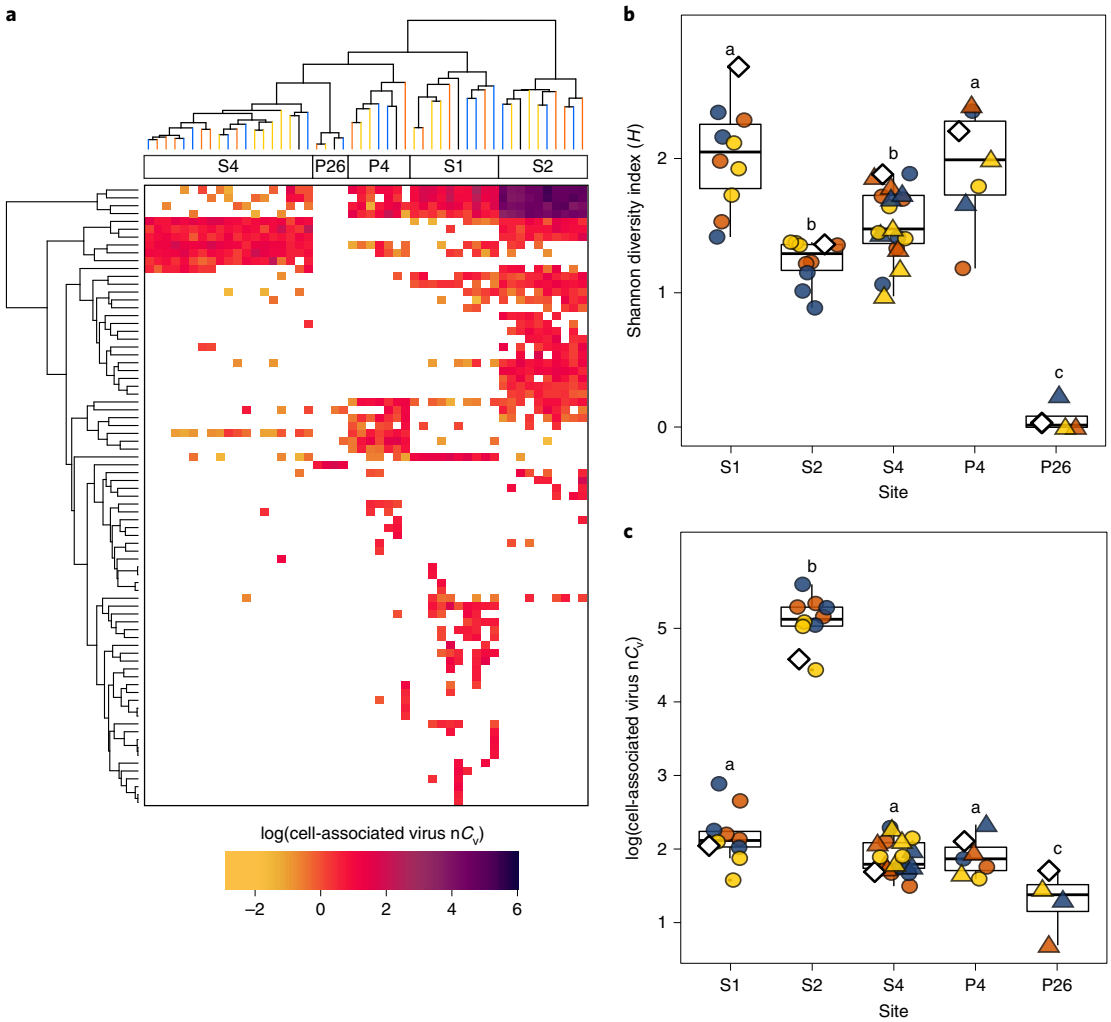


**Fig. 2 | Metatranscriptomic analysis of cell-associated diatom viruses. a**, Heatmap of diatom virus contig abundance across sites and incubations. Dendrograms reflect hierarchical clustering (rows, contigs; columns, samples coloured by treatment). White denotes contigs below detection. **b**,**c**, Shannon diversity index (*H*; **b**) and sum total of diatom virus contigs (**c**) at each site. Boxes depict median, upper and lower quartiles; whiskers denote values 1.5× the interquartile range. Symbols represents individual samples from Ctrl (yellow), DFB (blue) and +Fe (orange) treatments. Shape denotes timepoints (diamonds, $t_0$; circles, $t_1$ = 24–48 h; triangles, $t_2$ = 48–96 h). Letters denote statistically significant groups (ANOVA and Tukey's HSD post-hoc test; Supplementary Data 2).

suggesting Fe addition facilitated virus replication. Taken together, these data support the hypothesis that the onset of Fe limitation impairs viral replication in an actively infected diatom assemblage.

## Impaired viral infection in an Fe-limited model diatom

To directly test whether Fe limitation and its associated subcellular response disrupts viral replication, we grew and infected laboratory cultures of the cosmopolitan, bloom-forming diatom, *Chaetoceros tenuissimus*, under Fe-limiting conditions. Fe limitation was diagnosed by a decrease in specific growth rates, chlorophyll autofluorescence and electron transport rates, and further confirmed by +Fe 'rescue' experiments (Extended Data Fig. 6). Fe-limited cells were also characterized by a 51.4% increase in cellular $bSiO_2$ (Extended Data Fig. 6), consistent with previous work documenting increased silica production under Fe limitation[35,36]. In addition, Fe limitation also resulted in a 51.1% increase in bulk cellular antioxidant capacity (Extended Data Fig. 6), consistent with previous work demonstrating an enhanced ability of Fe-limited diatoms to combat oxidative stress[32,33,37].

When replete cultures were infected with the ssDNA virus, CtenDNAV, diatom host abundance decreased dramatically 5 days post infection (dpi) along with a marked increase in the proportion of dead cells (Fig. 4a). In contrast, when Fe-limited cultures were infected, the decline in host abundance was much more gradual and only apparent 8 dpi (Fig. 4a). A ~600-fold increase in extracellular virions was apparent in replete cultures 2 dpi ('pre-lysis'), compared with only a ~10-fold increase in Fe-limited cultures, indicating that early viral production was significantly impaired by Fe limitation in *C. tenuissimus* (Fig. 4b). In addition, the final viral titre ('post-lysis'), collected after host lysis, and burst size (the number of viruses produced per host cell) was significantly attenuated in Fe-limited cells compared with replete cells (Fig. 4b,c). Delayed host mortality was also observed in Fe-limited *C. tenuissimus* infected with a ssRNA virus, CtenRNAV (Extended Data Fig. 7), demonstrating a conserved response to these genetically distinct viruses. These data demonstrate impaired viral replication, reduced extracellular virus production and delayed host mortality under Fe limitation, and are consistent with previous work demonstrating decreased viral production in Fe-limited cultures of the green alga, *Micromonas*, and the prymnesiophyte, *Phaeocystis*[38].

Our observations of upregulated antioxidant genes in Fe-limited diatom communities (Fig. 3) and elevated cellular antioxidant

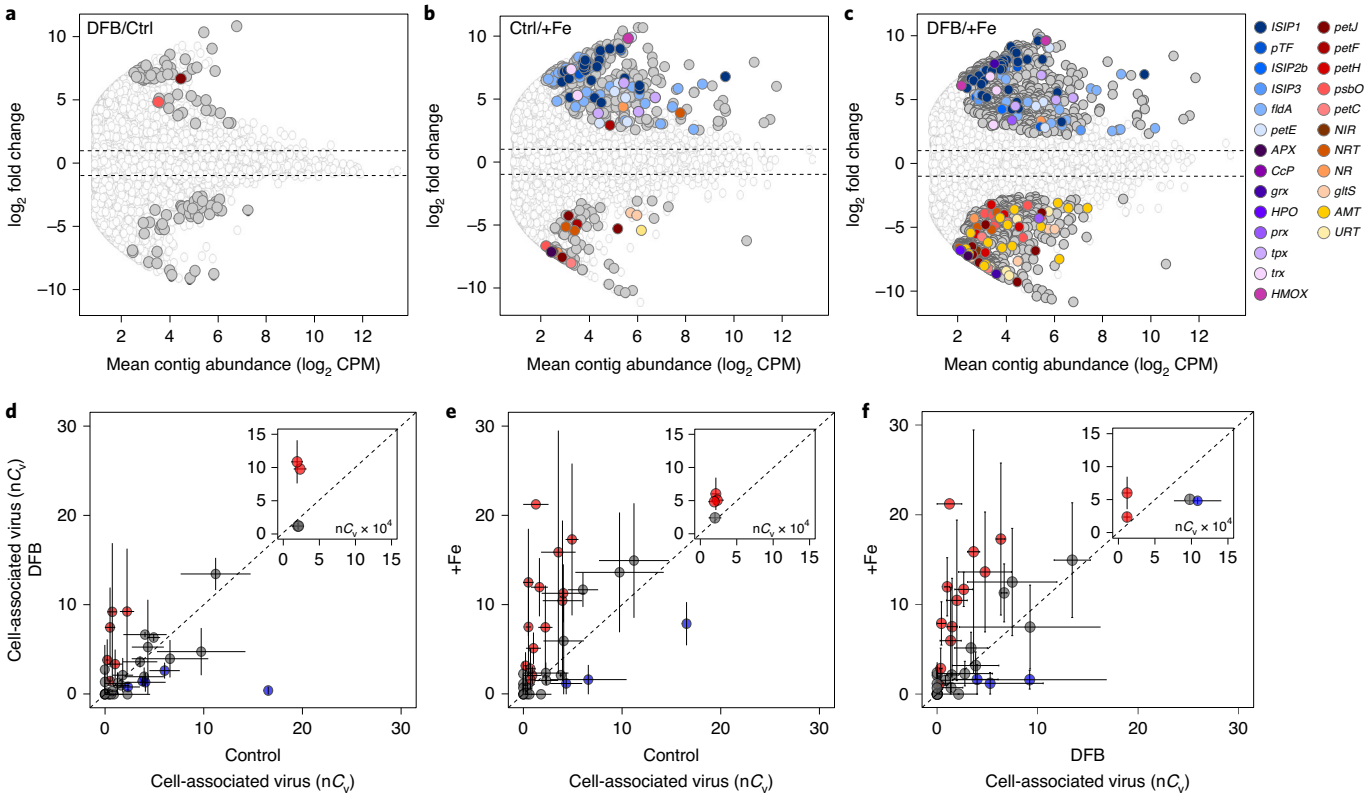


**Fig. 3 | Diatom molecular response and cell-associated diatom virus abundance during Fe limitation at S2. a–c**, Differential expression of diatom contigs as a function of mean contig abundance between DFB/Ctrl (**a**), Ctrl/+Fe (**b**) and DFB/+Fe (**c**). Filled symbols are statistically significant (FDR < 0.05). Colours denote genes involved in Fe limitation (blue), antioxidant activity (purple), photosynthesis (red) and nitrogen assimilation (orange/yellow). See Methods for abbreviations. **d–f**, Pairwise comparisons of cell-associated diatom virus contig abundance (mean ± standard error, $n = 3$) between DFB/Ctrl (**d**) +Fe/Ctrl (**e**) and +Fe/DFB (**f**) at $t_{48}$. Insets show highly abundant contigs. Colour denotes ≥2-fold increase (red) or decrease (blue). Unity slopes (dashed lines) indicate no difference.

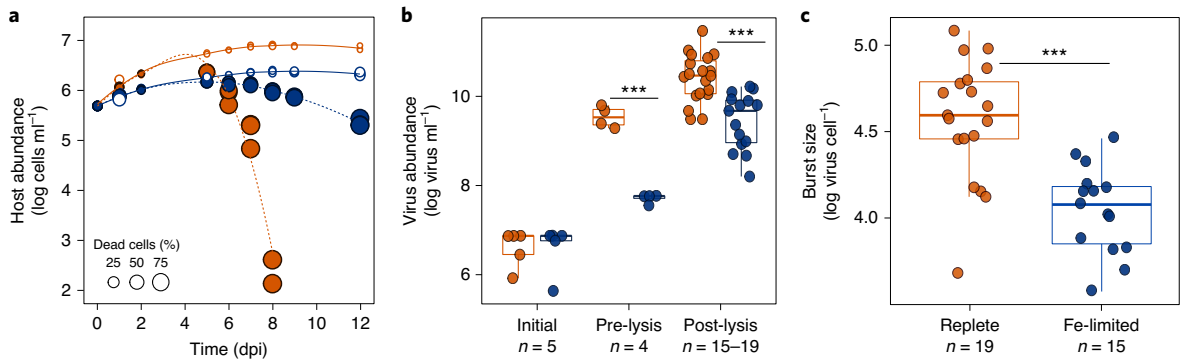


**Fig. 4 | Diatom host–virus dynamics in Fe-limited *C. tenuissimus*. a**, Host abundance and percent dead cells (symbol size) in replete (orange) and Fe-limited (blue), uninfected (open) and infected (filled) cultures with CtenDNAV (biological triplicates with LOESS regression). **b**, Virus abundance in replete (orange) and Fe-limited (blue) cultures at $t_0$ (initial), 2 dpi (pre-lysis) and post-lysis (6–8 days for replete; 8–12 days for Fe-limited). ***$P < 0.001$, two-way ANOVA, Tukey's HSD post-hoc test. **c**, Viral burst size in infected replete and Fe-limited cultures. Boxes depict median (line), upper and lower quartiles; whiskers denote values 1.5× the interquartile range. ***$P < 0.001$, unpaired two-tailed *t*-test.

capacity in Fe-limited *C. tenuissimus* (Extended Data Fig. 6) suggest the mechanism underlying this response may lie at the intersection of Fe homeostasis and reactive oxygen species (ROS) metabolism. Both Fe-dependent[38–40] and ROS-dependant[41–43] impacts on infection dynamics have emerged as focal points in diverse host–virus systems, ranging from bacteria to humans. While the production of ROS is well-established as an early host defence response to pathogen invasion[41], recent work suggests that ROS production can also be co-opted by viruses to support viral replication and trigger cell death[42,43]. Intriguingly, *HMOX*, a significantly upregulated transcript in the Fe-limited treatments at S2 (Fig. 3), is also associated with substantial antiviral activity in diverse viral lineages through broad cytoprotective mechanisms and the inhibition of programmed cell death pathways[44]. In picornaviruses specifically, *HMOX* reduces

viral replication through the attenuation of virus-induced ROS production[44]. In nutrient-replete *C. tenuissimus*, we observed a two- to threefold increase in ROS production during viral infection, concomitant with a decrease in host abundance (Extended Data Fig. 8). We also found that priming the host antioxidant system with a sub-lethal dose of hydrogen peroxide ($H_2O_2$), a well-described ROS, resulted in delayed infection dynamics (Extended Data Fig. 8), similar to those observed during Fe limitation. We posit that efficient ROS scavenging due to elevated cellular antioxidant capacity contributes to reduced viral production and delayed mortality in Fe-limited diatoms.

## Biogeochemical implications

In the vast Fe-limited regions of the global ocean, diatom silica production[9,10], species composition[45], grazing[46] and reduced microbial mediated remineralization[6] have been invoked as mechanistic explanations for enhanced silica burial[11] and efficient diatom carbon export[6,8]. Viruses, the most abundant biological entity in the ocean, are regarded as widespread mediators of remineralization and nutrient recycling. However, the discovery that environmental conditions such as temperature, salinity[47] or light[48] influence host–virus dynamics and the emerging concept of a 'viral shuttle' are transforming our view of viruses within a global biogeochemical framework[49]. Reduced viral replication and delayed mortality in Fe-limited diatoms, together with our previous findings that silicon limitation facilitates infection and accelerates mortality[18], highlight the fundamental imprint that nutrient availability has on host–virus interactions. Notably, our observations encompass both open ocean and coastal assemblages, experiencing chronic or transient Fe limitation, and allude to a shared cellular response that impedes infection even in regions with co-occurring Si limitation[50], establishing an 'ecophysiological hierarchy' with the impact of Fe superseding that of Si.

We suggest these dynamic, nutrient-driven host–virus interactions shape the fate of diatom carbon, silica and associated elements. Whereas diatoms infected in Si-limited regimes would enter the 'viral shunt', diatoms in Fe- or Fe/Si co-limited regimes would be retained in the particulate fraction and poised to enter the 'viral shuttle'. Impaired infection in Fe-limited diatoms, concomitant with increased mineral ballast, would further promote export, curbing the supply of carbon, nutrients and trace metals that would otherwise be released through lysis in the surface ocean.

## Online content

Any methods, additional references, Nature Research reporting summaries, source data, extended data, supplementary information, acknowledgements, peer review information; details of author contributions and competing interests; and statements of data and code availability are available at https://doi.org/10.1038/s41561-021-00711-6.

Received: 15 July 2020; Accepted: 10 February 2021;
Published online: 01 April 2021

## References

1. Nelson, D. M., Tréguer, P., Brzezinski, M. A., Leynaert, A. & Quéguiner, B. Production and dissolution of biogenic silica in the ocean: revised global estimates, comparison with regional data and relationship to biogenic sedimentation. *Glob. Biogeochem. Cycles* **9**, 359–372 (1995).
2. Smetacek, V. et al. Deep carbon export from a Southern Ocean iron-fertilized diatom bloom. *Nature* **487**, 313–319 (2012).
3. Hutchins, D. A., DiTullio, G. R., Zhang, Y. & Bruland, K. W. An iron limitation mosaic in the California upwelling regime. *Limnol. Oceanogr.* **43**, 1037–1054 (1998).
4. Bruland, K. W., Rue, E. L. & Smith, G. J. Iron and macronutrients in California coastal upwelling regimes: implications for diatom blooms. *Limnol. Oceanogr.* **46**, 1661–1674 (2001).
5. Boyd, P. W. et al. Mesoscale iron enrichment experiments 1993–2005: synthesis and future directions. *Science* **315**, 612–617 (2007).
6. Brzezinski, M. A. et al. Enhanced silica ballasting from iron stress sustains carbon export in a frontal zone within the California Current. *J. Geophys. Res. Oceans* **120**, 4654–4669 (2015).
7. Arteaga, L. A., Pahlow, M., Bushinsky, S. M. & Sarmiento, J. L. Nutrient controls on export production in the Southern Ocean. *Glob. Biogeochem. Cycles* **33**, 942–956 (2019).
8. Stukel, M. R. & Barbeau, K. A. Investigating the nutrient landscape in a coastal upwelling region and its relationship to the biological carbon pump. *Geophys. Res. Lett.* **47**, e2020GL087351 (2020).
9. Hutchins, D. A. & Bruland, K. W. Iron-limited diatom growth and Si:N uptake ratios in a coastal upwelling regime. *Nature* **393**, 561–564 (1998).
10. Takeda, S. Influence of iron availability on nutrient consumption ratio of diatoms in oceanic waters. *Nature* **393**, 774–777 (1998).
11. Pichevin, L. E., Ganeshram, R. S., Geibert, W., Thunell, R. & Hinton, R. Silica burial enhanced by iron limitation in oceanic upwelling margins. *Nat. Geosci.* **7**, 541–546 (2014).
12. Brzezinski, M. A. et al. A switch from $Si(OH)_4$ to $NO_3^-$ depletion in the glacial Southern Ocean. *Geophys. Res. Lett.* **29**, 1564 (2002).
13. Matsumoto, K., Sarmiento, J. L. & Brzezinski, M. A. Silicic acid leakage from the Southern Ocean: a possible explanation for glacial atmospheric $pCO_2$. *Glob. Biogeochem. Cycles* **16**, 1031 (2002).
14. Sarmiento, J. L., Gruber, N., Brzezinski, M. A. & Dunne, J. P. High-latitude controls of thermocline nutrients and low latitude biological productivity. *Nature* **427**, 56–60 (2004).
15. Fuhrman, J. A. Marine viruses and their biogeochemical and ecological effects. *Nature* **399**, 541–548 (1999).
16. Suttle, C. A. Marine viruses—major players in the global ecosystem. *Nat. Rev. Microbiol.* **5**, 801–812 (2007).
17. Wilhelm, S. W. & Suttle, C. A. Viruses and nutrient cycles in the sea: viruses play critical roles in the structure and function of aquatic food webs. *Bioscience* **49**, 781–788 (1999).
18. Kranzler, C. F. et al. Silicon limitation facilitates virus infection and mortality of marine diatoms. *Nat. Microbiol.* **4**, 1790–1797 (2019).
19. Laber, C. P. et al. *Coccolithovirus* facilitation of carbon export in the North Atlantic. *Nat. Microbiol.* **3**, 537–547 (2018).
20. Yamada, Y., Tomaru, Y., Fukuda, H. & Nagata, T. Aggregate formation during the viral lysis of a marine diatom. *Front. Mar. Sci.* **5**, 167 (2018).
21. Pelusi, A. et al. Virus-induced spore formation as a defense mechanism in marine diatoms. *New Phytol.* **229**, 2251–2259 (2020).
22. Johnson, K. S., Chavez, F. P. & Friederich, G. E. Continental-shelf sediment as a primary source of iron for coastal phytoplankton. *Nature* **398**, 697–700 (1999).
23. Harrison, P. J. Station Papa time series: insights into ecosystem dynamics. *J. Oceanogr.* **58**, 259–264 (2002).
24. Marchetti, A. et al. Development of a molecular-based index for assessing iron status in bloom-forming pennate diatoms. *J. Phycol.* **53**, 820–832 (2017).
25. Cohen, N. R. et al. Diatom transcriptional and physiological responses to changes in iron bioavailability across ocean provinces. *Front. Mar. Sci.* **4**, 360 (2017).
26. Lampe, R. H. et al. Different iron storage strategies among bloom-forming diatoms. *Proc. Natl Acad. Sci. USA* **115**, E12275–E12284 (2018).
27. King, A. L. & Barbeau, K. Evidence for phytoplankton iron limitation in the southern California Current System. *Mar. Ecol. Prog. Ser.* **342**, 91–103 (2007).
28. Boyd, P. & Harrison, P. J. Phytoplankton dynamics in the NE subarctic Pacific. *Deep Sea Res. II* **46**, 2405–2432 (1999).
29. Till, C. P. et al. The iron limitation mosaic in the California Current System: factors governing Fe availability in the shelf/near-shelf region. *Limnol. Oceanogr.* **64**, 109–123 (2019).
30. Gozzelino, R., Jeney, V. & Soares, M. P. Mechanisms of cell protection by heme oxygenase-1. *Annu. Rev. Pharmacol. Toxicol.* **50**, 323–354 (2010).
31. Richaud, C. & Zabulon, G. The heme oxygenase gene (*pbsA*) in the red alga *Rhodella violacea* is discontinuous and transcriptionally activated during iron limitation. *Proc. Natl Acad. Sci. USA* **94**, 11736–11741 (1997).
32. Allen, A. E. et al. Whole-cell response of the pennate diatom *Phaeodactylum tricornutum* to iron starvation. *Proc. Natl Acad. Sci. USA* **105**, 10438–10443 (2008).
33. Thamatrakoln, K., Korenovska, O., Niheu, A. K. & Bidle, K. D. Whole-genome expression analysis reveals a role for death-related genes in stress acclimation of the diatom *Thalassiosira pseudonana*. *Environ. Microbiol.* **14**, 67–81 (2012).
34. Marchetti, A. et al. Comparative metatranscriptomics identifies molecular bases for the physiological responses of phytoplankton to varying iron availability. *Proc. Natl Acad. Sci. USA* **109**, E317–E325 (2012).
35. De La Rocha, C. L., Hutchins, D. A., Brzezinski, M. A. & Zhang, Y. Effects of iron and zinc deficiency on elemental composition and silica production by diatoms. *Mar. Ecol. Prog. Ser.* **195**, 71–79 (2000).
36. Leynaert, A. et al. Effect of iron deficiency on diatom cell size and silicic acid uptake kinetics. *Limnol. Oceanogr.* **49**, 1134–1143 (2004).

37. van Creveld, S. G., Rosenwasser, S., Levin, Y. & Vardi, A. Chronic iron limitation confers transient resistance to oxidative stress in marine diatoms. *Plant Physiol.* **172**, 968–979 (2016).
38. Slagter, H. A., Gerringa, L. J. A. & Brussaard, C. P. D. Phytoplankton virus production negatively affected by iron limitation. *Front. Mar. Sci.* **3**, 156 (2016).
39. Drakesmith, H. & Prentice, A. Viral infection and iron metabolism. *Nat. Rev. Microbiol.* **6**, 541–552 (2008).
40. Weinbauer, M. G., Arrieta, J. M., Griebler, C. & Herndlb, G. J. Enhanced viral production and infection of bacterioplankton during an iron-induced phytoplankton bloom in the Southern Ocean. *Limnol. Oceanogr.* **54**, 774–784 (2009).
41. Torres, M. A., Jones, J. D. G. & Dangl, J. L. Reactive oxygen species signaling in response to pathogens. *Plant Physiol.* **141**, 373–378 (2006).
42. Sheyn, U., Rosenwasser, S., Ben-Dor, S., Porat, Z. & Vardi, A. Modulation of host ROS metabolism is essential for viral infection of a bloom-forming coccolithophore in the ocean. *ISME J.* **10**, 1742–1754 (2016).
43. Hyodo, K., Hashimoto, K., Kuchitsu, K., Suzuki, N. & Okuno, T. Harnessing host ROS-generating machinery for the robust genome replication of a plant RNA virus. *Proc. Natl Acad. Sci. USA* **114**, E1282–E1290 (2017).
44. Espinoza, J. A., Gonzalez, P. A. & Kalergis, A. M. Modulation of antiviral immunity by heme oxygenase-1. *Am. J. Pathol.* **187**, 487–493 (2017).
45. Durkin, C. A. et al. Frustule-related gene transcription and the influence of diatom community composition on silica precipitation in an iron-limited environment. *Limnol. Oceanogr.* **57**, 1619–1633 (2012).
46. Assmy, P. et al. Thick-shelled, grazer-protected diatoms decouple ocean carbon and silicon cycles in the iron-limited Antarctic Circumpolar Current. *Proc. Natl Acad. Sci. USA* **110**, 20633–20638 (2013).
47. Kimura, K. & Tomaru, Y. Effects of temperature and salinity on diatom cell lysis by DNA and RNA viruses. *Aquat. Microb. Ecol.* **79**, 79–83 (2017).
48. Thamatrakoln, K. et al. Light regulation of coccolithophore host–virus interactions. *New Phytol.* **221**, 1289–1302 (2019).
49. Zimmerman, A. E. et al. Metabolic and biogeochemical consequences of viral infection in aquatic ecosystems. *Nat. Rev. Microbiol.* **18**, 21–34 (2020).
50. Brzezinski, M. A. et al. Co-limitation of diatoms by iron and silicic acid in the equatorial Pacific. *Deep Sea Res. II* **58**, 493–511 (2011).

## Methods

**Cruise sampling and measurements.** Incubation experiments were conducted on two separate cruises—one within the CUZ, 3–26 July 2014, onboard the RV *Melville* (MV1405) and another along Line P in the subarctic northeast Pacific Ocean, 7–23 June 2015, onboard the Canadian Coast Guard Ship *John P. Tully* (Line P cruise 2015-09). Details on incubation setup are reported elsewhere[25,26]. Briefly, surface water collected using trace-metal-clean techniques was distributed into acid-cleaned 10 l cubitainers. Treatments, in triplicate, included an unamended control (Ctrl), a 200 nM addition of DFB to bind and reduce bioavailable iron, and the addition of 5 nM $FeCl_3$ (+Fe). At site S2, 15 µM of $Si(OH)_4$ was added to all treatments to support growth of diatoms due to the initially low $Si(OH)_4$ concentration (<4.7 µM). At site P4, 10 µM of $NO_3^-$ was added to all treatments to support growth due to low initial $NO_3^-$ concentrations (<1.5 µM). Cubitainers were incubated on deck with flowing surface seawater for temperature control and screened to approximately 30% surface irradiance and sampled at dawn. Each site was sampled at the start of the incubation (initial, $t_0$) and at two timepoints ($t_1$ and $t_2$) throughout each experiment (24 and 48 h at S1; 48 and 72 h at S2; 48 h and 72 h at S4; 24 h and 48 h at P4; 48 and 96 h at P26). Methods for analysing chl *a*, $bSiO_2$, photosynthetic efficiency, and dissolved nutrients and iron are described elsewhere[25]. Mean surface nitrate concentrations shown in Fig. 1a were obtained from the World Ocean Database[51].

Silica production rates were measured using the radioisotope $^{32}Si$ as described in ref. [52]; 320 ml samples received 260 Bq $^{32}Si(OH)_4$ (specific activity >40 kBq (µg $Si)^{-1}$) followed by incubation in deckboard flow-through incubators screened with neutral density filters to 55% of surface irradiance. After 4–7 h, samples were filtered onto 1.2 µm polycarbonate filters (Millipore) and quantified as described in ref. [53]. Gross production rates ($\rho$ in µM Si $d^{-1}$) were normalized to $bSiO_2$ concentration to determine specific rates[54] ($V_b$ $d^{-1}$). Si stress was assessed using paired samples that measured silica production rates at the ambient silicic acid concentration ($V_{amb}$) and after an 18 µM addition of non-radioactive sodium silicate ($V_{enh}$). Under the assumption that the 18 µM $Si(OH)_4$ addition saturates $Si(OH)_4$ uptake (that is, approximates the maximum uptake rate, $V_{max}$), the ratio $V_{amb}$:$V_{enh}$ represents the fraction of maximum uptake rate supported by the ambient [$Si(OH)_4$][55], with values of ~1 indicative of Si-replete populations and values approaching zero indicative of severe Si stress. Values between 0.92 and 1.0 are considered within the error of detection[56].

**Metatranscriptomic analysis.** Biomass for metatranscriptomic analysis was collected by filtration onto 0.8 µm Pall Supor filters (142 mm) via peristaltic pumping, immediately flash frozen in liquid $N_2$ and stored at −80 °C until extraction onshore. Biomass samples were collected at the start of the incubation (initial, $t_0$) and at 24 h (S1), 48 h (S2), 48 h and 72 h (S4), 24 h and 48 h (P4), and 96 h (P26). The initial RNA extraction, sequencing, assemblies and annotations are described elsewhere[25,26]. Briefly, RNA was extracted using the ToTALLY RNA Total RNA Isolation Kit (Ambion Thermo Fisher Scientific). Metatranscriptomic library preparation was performed with the Illumina TruSeq Stranded mRNA Library Preparation Kit and HiSeq v4 reagents with poly-A selection of mRNA. Samples were barcoded and sequenced on an Illumina HiSeq 2000. Biological triplicates were sequenced for each treatment, except for samples with low yields (for example, $t_0$ and Line P samples), in which triplicates were pooled into one sample. Merged pairs and non-overlapping paired-end reads were used to assemble contigs using ABySS v1.5.2 with varied *k*-mer sizes[57]. Subassemblies from each site were merged with Trans-ABySS v1.5.3[58] and redundant contig removal verified with GenomeTools v1.5.1[59]. Only contigs with 100% identity were merged. In cases where a shorter contig was contained within a longer contig and 100% identical, the longer contig was retained. Contigs shorter than 120 bp were discarded. Functional annotation of eukaryotic transcripts was assigned by best homology (lowest *E* value) with BLASTX v2.2.31 and the Kyoto Encyclopedia of Genes and Genomes (release 75)[60]. Taxonomic classification and additional functional annotation of hypothetical proteins were assigned using MarineRefII, a custom reference database maintained by the Moran Lab at the University of Georgia that includes transcriptomes from the Marine Microbial Eukaryote Transcriptome Sequencing Project[61]. Read counts were estimated from the merged assembly containing contigs from all sites and incubations using the quasi-mapping method implemented in Salmon v0.73[62]. No pre-filtering of reads was performed—contigs with normalized counts >0 were considered to be present. In our analysis of relative transcript abundance, major eukaryotic phytoplankton taxa and diatom genera that were <5% of the total mapped reads were classified as 'other'.

Downstream metatranscriptomic analyses were performed in the open source program R version 3.5.1 Feather Spray[63]. *Ps-n* ILI values were calculated as described in ref. [24]. For sites S1 and P26, the index was calculated from unamended deckboard incubations, due to low initial abundance of *Pseudo-nitzschia* transcripts. For analysis of diatom transcript abundance, EdgeR v3.12.0[64] was used to calculate the mean counts per million (CPM) and fold change of diatom transcripts in pairwise comparisons between treatments, using the exactTest with edgeR's estimate of tagwise dispersion across all samples. *P* values were adjusted for multiple testing with the FDR-controlling procedure[65] and FDR = 0.05 was used as the cutoff for differentially expressed genes. Log fold change (M) versus mean abundance (A) plots were produced using the R package ggplot2[66]. Abbreviations for analysed contigs are as follows: iron starvation induced protein 1 (*ISIP1*), phytotransferrin (*pTF*, formerly *ISIP2a*), iron starvation induced protein 2B (*ISIP2b*), iron starvation induced protein 3 (*ISIP3*), flavodoxin (*fldA*), plastocyanin (*petE*), ascorbate peroxidase (*APX*), cytochrome c peroxidase (*CcP*), glutaredoxin (*grx*), haloperoxidase (*HPO*), haem oxygenase (*HMOX*), peroxiredoxin (*prx*), thioredoxin-dependent peroxiredoxin (*tpx*), thioredoxin (*trx*), ferredoxin (*petF*), ferredoxin-NADP + reductase (*petH*), cytochrome $c_6$ (*petJ*), photosystem II oxygen-evolving enhancer (*psbO*), cytochrome $b_6f$ (*petC*), nitrate transporter (*NRT*), nitrate reductase (*NR*), nitrite reductase (*NIR*), glutamate synthase (*gltS*), urea transporter (*URT*) and ammonium transporter (*AMT*).

Diatom virus contigs were identified using a homology-based query (TBLASTN, *E* value < $10^{-3}$) with RdRp and Rep genes from known diatom-infecting ssRNA (family *Marnaviridae*) and ssDNA viruses (family *Bacilladnaviridae*), respectively. Given the poly-A tailed genomes of ssRNA diatom viruses, poly-A selection during metatranscriptomic library preparation would capture ssRNA viral genomes as well as actively replicating viruses. Diatom virus RdRp read counts were normalized to the length of each contig and sequencing depth yielding viral contigs per million ($C_v$), analogous to transcript per million normalization[67] used for comparing relative gene expression between samples. To assess the degree of infection across samples with different diatom biomass loads, $C_v$ was normalized to total diatom transcript per million[18], to yield normalized cell-associated diatom virus contig abundance ($nC_v$), similar to group normalization methods used in previous studies[34,68,69]. The use of total diatom transcript abundance as a proxy for diatom biomass was previously validated as an indicator of diatom biomass using microscope counts and bulk measurements[26]. Heatmaps and dendrograms using Euclidean distance and hierarchical clustering were produced with the R package gplots v3.0.1.2[70]. Shannon diversity indices for diatom virus diversity were calculated using the R package vegan[71].

For phylogenetic analysis of viral contigs, reference *Picornavirales* RdRp amino acid sequences were obtained from the National Center for Biotechnology Information, trimmed and aligned using ClustalW[72] in Mega 7[73]. A maximum likelihood tree was constructed from the reference alignment using RAxML v8.2.10 with the PROTGAMMAWAGF substitution model and 100 bootstrap replicates[74]. Putative diatom virus contigs (*E* value < $10^{-3}$) were aligned to the reference alignment using hmmalign and the hidden Markov model (HMM) profile of the reference alignment (built using hmmbuild in HMMER; hmmer.org). Tree files were packaged using taxtastic v0.8.3 and environmental contigs were placed on the reference tree using pplacer v1.1.alpha19[75]. The tree was exported and the posterior probability was calculated using guppy v1.1[75].

**Culturing conditions and infection experiments.** *Chaetoceros tenuissimus* Meunier, isolated in the coastal waters of Japan[76], and its associated viruses were kindly provided by Y. Tomaru (National Research Institute of Fisheries and Environment of Inland Sea, Japan). Host cultures were maintained in modified SWM-3 media[77] with 0.2 mM silicate, 2 mM nitrate and 2 nM $Na_2SeO_3$[76], at 15 °C on a 12:12 light:dark cycle at ~120 µmol photons $m^{-2}$ $s^{-1}$. Culture work was performed in sterile polystyrene filter-capped culture flasks or in acid-washed polycarbonate culture flasks to minimize iron contamination. Cell abundance was measured by flow cytometry (BD Accuri C6; 488 nm excitation, >670 nm emission) using chlorophyll fluorescence and forward scatter.

For Fe-limitation experiments, exponentially growing cultures in replete media were centrifuged at 4,000 × *g* for 10 min and washed and resuspended in either SWM-3 without added Fe or in an artificial seawater media[78,79] (ESAW) without added iron and buffered with 100 µM EDTA[80]. Once an Fe-limited phenotype was confirmed (~3–5 days), cultures were subdivided and one set was infected with CtenDNAV[81] or CtenRNAV[76] at a multiplicity of infection of 10. Data shown are representative of five independent experiments ($n = 15$). For experiments with hydrogen peroxide ($H_2O_2$), a sub-lethal concentration was determined using a dose curve of 0–150 µM $H_2O_2$ (Sigma; 30% v/v) on exponentially growing cultures (~$4.5 \times 10^5$ cells $ml^{-1}$). Cell abundance and photosynthetic efficiency were monitored and 100 µM $H_2O_2$ was selected for downstream infection experiments. For infection experiments following $H_2O_2$ addition, viruses were added to cultures 24 h after exposure to 100 µM $H_2O_2$. All statistical analyses of data collected from laboratory cultures were performed in R version 3.5.1 Feather Spray[63].

**Cellular biogenic silica and particulate organic carbon.** Dissolved silicon and $bSiO_2$ in laboratory cultures were measured using standard protocols[82,83]. Samples for particulate organic carbon measurements were collected on pre-combusted GF/F filters, wrapped in pre-combusted foil and stored at −20 °C until processing. Filters were thawed and dried at 60 °C and then placed in a glass desiccator with concentrated hydrochloric acid for 24 h to dissolve particulate inorganic carbon. Samples were analysed on a CNS elemental analyser (Carlo Erba NA 1500).

**Biophysical measurements.** Maximum photochemical quantum yield of photosystem II (photosynthetic efficiency; $F_v/F_m$) was measured using a custom-built fluorescence induction and relaxation system[84], providing measurements of $F_o$ (minimum) and $F_m$ (maximum) fluorescence yields. Maximum efficiency of photosystem II was calculated as the ratio between variable fluorescence ($F_v$) and $F_m$, where $F_v/F_m = (F_m - F_o)/F_m$. Prior to measurements,

cultures were acclimated in low light for 15 min. Maximal rates of photosynthetic electron transport ($P_{max}$) were retrieved by fitting photosynthesis versus irradiance curves with the exponential rise function, $P = P_{max}(1 - \exp(E/E_k))$, where $E$ is the irradiance and $E_k$ is the light saturation parameter.

**Cellular antioxidant capacity.** Fe-limited and replete cultures were collected by filtration on 1.2 µm polycarbonate membrane filters and resuspended in buffer (5 mM potassium phosphate, 0.9% sodium chloride, pH = 7.4). Cells lysates were generated through three flash freeze–sonication cycles (30 sec sonication on ice). Samples were then centrifuged at 10,000 × *g* at 4 °C for 15 min to collect cell debris and supernatants were transferred to fresh tubes and stored at −80 °C until further analysis. The total antioxidant capacity in cell extracts was determined using the antioxidant assay kit (Cayman Chemical), according to the manufacturer's instructions. Absorbance at 750 nm was measured in a SpectraMax M3 microplate reader and the cellular antioxidant capacity is expressed as Trolox equivalents (mM per cell).

**Diagnostic staining and flow cytometry.** The relative proportion of live/dead cells in cultures was determined by staining with SYTOX Green (Thermo Fisher Scientific) at a final concentration of 1 µM for 15 min in the dark at room temperature and subsequent analysis using flow cytometry (BD Accuri C6; 488 nm excitation, 533/30 emission). Unstained samples were used to set a threshold for background green fluorescence. The relative number of dead cells in a population (percent positively stained) was determined as those that exceeded the background fluorescence of the unstained sample. Intracellular ROS were determined by staining with 2′,7′–dichlorodihydrofluorescein diacetate (CM–$H_2$DCFDA; Thermo Fisher Scientific) at a final concentration of 5 µM for 1 h in the dark at room temperature and subsequent analysis using flow cytometry (BD Accuri C6; 488 nm excitation, 533/30 emission). Intracellular ROS fluorescence was calculated by subtracting the mean background cellular fluorescence of unstained populations (relative fluorescence units per cell) from the mean fluorescence of positively stained populations.

**Virus abundance.** Virus abundance was measured in lysates generated by filtering infected cultures through a 0.22 µm pore size filter to remove cellular debris. Lysates were stored at 4 °C and processed within one month of collection. The abundance of infectious virus particles (infectious units $ml^{-1}$) was measured using the most probable number assay[18,85] (MPN) and calculated using the EPA-MPN calculator[86]. Extracellular virus abundance data were collected from 2–6 independent experiments. Burst size was calculated by dividing the final virus abundance by the decrease in host abundance.

## Data availability

All cruise-related data are publicly available at the Biological & Chemical Oceanography Data Management Office (CUZ: project number 559966, https://www.bco-dmo.org/deployment/559966; Line P: http://www.waterproperties.ca/linep/2015-009/index.php). Metatranscriptome sequencing data are available in the NCBI sequence read archive (SRA) under the BioProject accession numbers PRJNA320398 and PRJNA388329. Assembled contigs, read counts and functional annotation of contigs are available at http://marchettilab.web.unc.edu/data. All data generated or analysed during this study are included in this published article and its Supplementary Information files. Source data are provided with this paper.

## References


51. Boyer, T. P. et al. *World Ocean Database 2013* (NOAA Atlas, 2013).
52. Krause, J. W. et al. The interaction of physical and biological factors drives phytoplankton spatial distribution in the northern California Current. *Limnol. Oceanogr.* **65**, 1974–1989 (2020).
53. Krause, J. W., Nelson, D. M. & Brzezinski, M. A. Biogenic silica production and the diatom contribution to primary production and nitrate uptake in the eastern equatorial Pacific Ocean. *Deep Sea Res. II* **58**, 434–448 (2011).
54. Brzezinski, M. A. & Phillips, D. R. Evaluation of $^{32}$Si as a tracer for measuring silica production rates in marine waters. *Limnol. Oceanogr.* **42**, 856–865 (1997).
55. Nelson, D. M., Brzezinski, M. A., Sigmon, D. E. & Franck, V. M. A seasonal progression of Si limitation in the Pacific sector of the Southern Ocean. *Deep Sea Res. II* **48**, 3973–3995 (2001).
56. Krause, J. W., Brzezinski, M. A., Villareal, T. A. & Wilson, C. Increased kinetic efficiency for silicic acid uptake as a driver of summer diatom blooms in the North Pacific subtropical gyre. *Limnol. Oceanogr.* **57**, 1084–1098 (2012).
57. Birol, I. et al. De novo transcriptome assembly with ABySS. *Bioinformatics* **25**, 2872–2877 (2009).
58. Robertson, G. et al. De novo assembly and analysis of RNA-seq data. *Nat. Methods* **7**, 909–912 (2010).
59. Gremme, G., Steinbiss, S. & Kurtz, S. GenomeTools: a comprehensive software library for efficient processing of structured genome annotations. *IEEE/ACM Trans. Comput. Biol. Bioinform.* **10**, 645–656 (2013).
60. Kanehisa, M., Furumichi, M., Tanabe, M., Sato, Y. & Morishima, K. KEGG: new perspectives on genomes, pathways, diseases and drugs. *Nucleic Acids Res.* **45**, D353–D361 (2017).
61. Keeling, P. J. et al. The Marine Microbial Eukaryote Transcriptome Sequencing Project (MMETSP): illuminating the functional diversity of eukaryotic life in the oceans through transcriptome sequencing. *PLoS Biol.* **12**, e1001889 (2014).
62. Patro, R., Duggal, G., Love, M. I., Irizarry, R. A. & Kingsford, C. Salmon provides fast and bias-aware quantification of transcript expression. *Nat. Methods* **14**, 417–419 (2017).
63. R Core Team *R: A Language and Environment for Statistical Computing* (R Foundation for Statistical Computing, 2013).
64. Robinson, M. D., McCarthy, D. J. & Smyth, G. K. EdgeR: a bioconductor package for differential expression analysis of digital gene expression data. *Bioinformatics* **26**, 139–140 (2010).
65. Benjamini, Y. & Hochberg, Y. Controlling the false discovery rate: a practical and powerful approach to multiple testing. *J. R. Stat. Soc. B* **57**, 289–300 (1995).
66. Wickham, H. *ggplot2: Elegant Graphics for Data Analysis* (Springer, 2016).
67. Wagner, G. P., Kin, K. & Lynch, V. J. Measurement of mRNA abundance using RNA-seq data: RPKM measure is inconsistent among samples. *Theory Biosci.* **131**, 281–285 (2012).
68. Alexander, H., Jenkins, B. D., Rynearson, T. A. & Dyhrman, S. T. Metatranscriptome analyses indicate resource partitioning between diatoms in the field. *Proc. Natl Acad. Sci. USA* **112**, E2182–E2190 (2015).
69. Lampe, R. H. et al. Divergent gene expression among phytoplankton taxa in response to upwelling. *Environ. Microbiol.* **20**, 3069–3082 (2018).
70. Warnes, G. R. et al. *gplots: Various R Programming Tools for Plotting Data* https://cran.r-project.org/web/packages/gplots/index.html (2019).
71. Oksanen, J. et al. *vegan: Community Ecology Package* https://cran.r-project.org/web/packages/vegan/index.html (2019).
72. Thompson, J. D., Higgins, D. G. & Gibson, T. J. CLUSTAL W: improving the sensitivity of progressive multiple sequence alignment through sequence weighting, position-specific gap penalties and weight matrix choice. *Nucleic Acids Res.* **22**, 4673–4680 (1994).
73. Kumar, S., Stecher, G. & Tamura, K. MEGA7: molecular evolutionary genetics analysis version 7.0 for bigger datasets. *Mol. Biol. Evol.* **33**, 1870–1874 (2016).
74. Stamatakis, A. RAxML version 8: a tool for phylogenetic analysis and post-analysis of large phylogenies. *Bioinformatics* **30**, 1312–1313 (2014).
75. Matsen, F. A., Kodner, R. B. & Armbrust, E. V. pplacer: linear time maximum-likelihood and Bayesian phylogenetic placement of sequences onto a fixed reference tree. *BMC Bioinform.* **11**, 538 (2010).
76. Shirai, Y. et al. Isolation and characterization of a single-stranded RNA virus infecting the marine planktonic diatom *Chaetoceros tenuissimus* Meunier. *Appl. Environ. Microbiol.* **74**, 4022–4027 (2008).
77. Chen, L.-M., Edelstein, T. & McLachlan, J. *Bonnemaisonia hamifera* Hariot in nature and in culture. *J. Phycol.* **5**, 211–220 (1969).
78. Harrison, P. J., Waters, R. E. & Taylor, F. J. R. A broad spectrum artificial sea water medium for coastal and open ocean phytoplankton. *J. Phycol.* **16**, 28–35 (1980).
79. Berges, J. A., Franklin, D. J. & Harrison, P. J. Evolution of an artificial seawater medium: improvements in enriched seawater, artificial water over the last two decades. *J. Phycol.* **37**, 1138–1145 (2001).
80. Sunda, W. G., Price, N. M. & Morel, F. M. M. Trace metal ion buffers and their use in culture studies. *Algal Cult. Tech.* **4**, 35–63 (2005).
81. Tomaru, Y., Shirai, Y., Toyoda, K. & Nagasaki, K. Isolation and characterization of a single-stranded DNA virus infecting the marine planktonic diatom *Chaetoceros tenuissimus*. *Aquat. Microb. Ecol.* **64**, 175–184 (2011).
82. Parsons, T. R. *A Manual of Chemical & Biological Methods for Seawater Analysis* (Elsevier, 2013).
83. Krause, J. W., Lomas, M. W. & Nelson, D. M. Biogenic silica at the Bermuda Atlantic time-series study site in the Sargasso Sea: temporal changes and their inferred controls based on a 15-year record. *Glob. Biogeochem. Cycles* **23**, GB3004 (2009).
84. Gorbunov, M. Y. & Falkowski, P. G. Fluorescence induction and relaxation (FIRe) technique and instrumentation for monitoring photosynthetic processes and primary production in aquatic ecosystems. In *Photosynthesis: Fundamental Aspects to Global Perspectives—Proc. 13th International Congress of Photosynthesis* (eds Van der Est, A. & Bruce, D.) 1029–1031 (Allen and Unwin, 2004).
85. Suttle, C. A. in *Handbook of Methods in Aquatic Microbial Ecology* (eds Kemp, P. F. et al.) 121–134 (CRC Press, 1993).
86. Klee, A. J. A computer program for the determination of most probable number and its confidence limits. *J. Microbiol. Methods* **18**, 91–98 (1993).


## Acknowledgements


We would like to thank the captain and the crew of the RV *Melville* (MV1405) and the Canadian Coast Guard Ship *J. P. Tully* (Line P 2015-09), as well as G. Smith, F. Kuzminov,

K. Ellis and T. Coale for technical assistance during the cruise. Thank you to Y. Tomaru for providing the laboratory diatom host-virus systems, K. Bondoc and B. Knowles for useful discussions on statistical analyses and K. D. Bidle for thoughtful feedback on the manuscript. This work was supported by grants from the National Science Foundation (OCE-1333929 to K.T., OCE-1334387 to M.A.B., OCE-1334935 to A.M., OCE-1259776 to K.W.B. and OCE-1334632 to B.S.T.) and a postdoctoral fellowship to C.F.K. from the Simons Foundation (SF 548156). Salary support for C.F.K. was also provided by the Institute of Earth, Ocean and Atmospheric Sciences at Rutgers University, the Rappaport Fund for Advanced Studies and Israel's Council for Higher Education.

## Author contributions

C.F.K. and K.T. conceived the project, designed the laboratory experiments and wrote the manuscript. C.F.K. performed metatranscriptome and statistical analyses. C.F.K. conducted the laboratory culture-based experiments. J.M. and J.R.L. provided technical support on laboratory experiments. M.M. assisted with RdRp phylogenetic analyses. K.T., M.A.B., N.R.C., M.M., C.P.T., A.M., B.S.T. and K.W.B. participated, collected and analysed samples on the CUZ cruise; B.S.T. and N.R.C. participated, collected and analysed samples on the Line P cruise. A.M., N.R.C. and R.H.L. extracted the RNA and generated the metatranscriptome data. All authors provided comments on the manuscript.

## Competing interests

The authors declare no competing interests.

## Additional information

**Extended data** is available for this paper at https://doi.org/10.1038/s41561-021-00711-6.

**Supplementary information** The online version contains supplementary material available at https://doi.org/10.1038/s41561-021-00711-6.

**Correspondence and requests for materials** should be addressed to C.F.K. or K.T.

**Peer review information** *Nature Geoscience* thanks Erin Bertrand, Alex Poulton and the other, anonymous, reviewer(s) for their contribution to the peer review of this work. Primary Handling Editors: Clare Davis; Xujia Jiang.

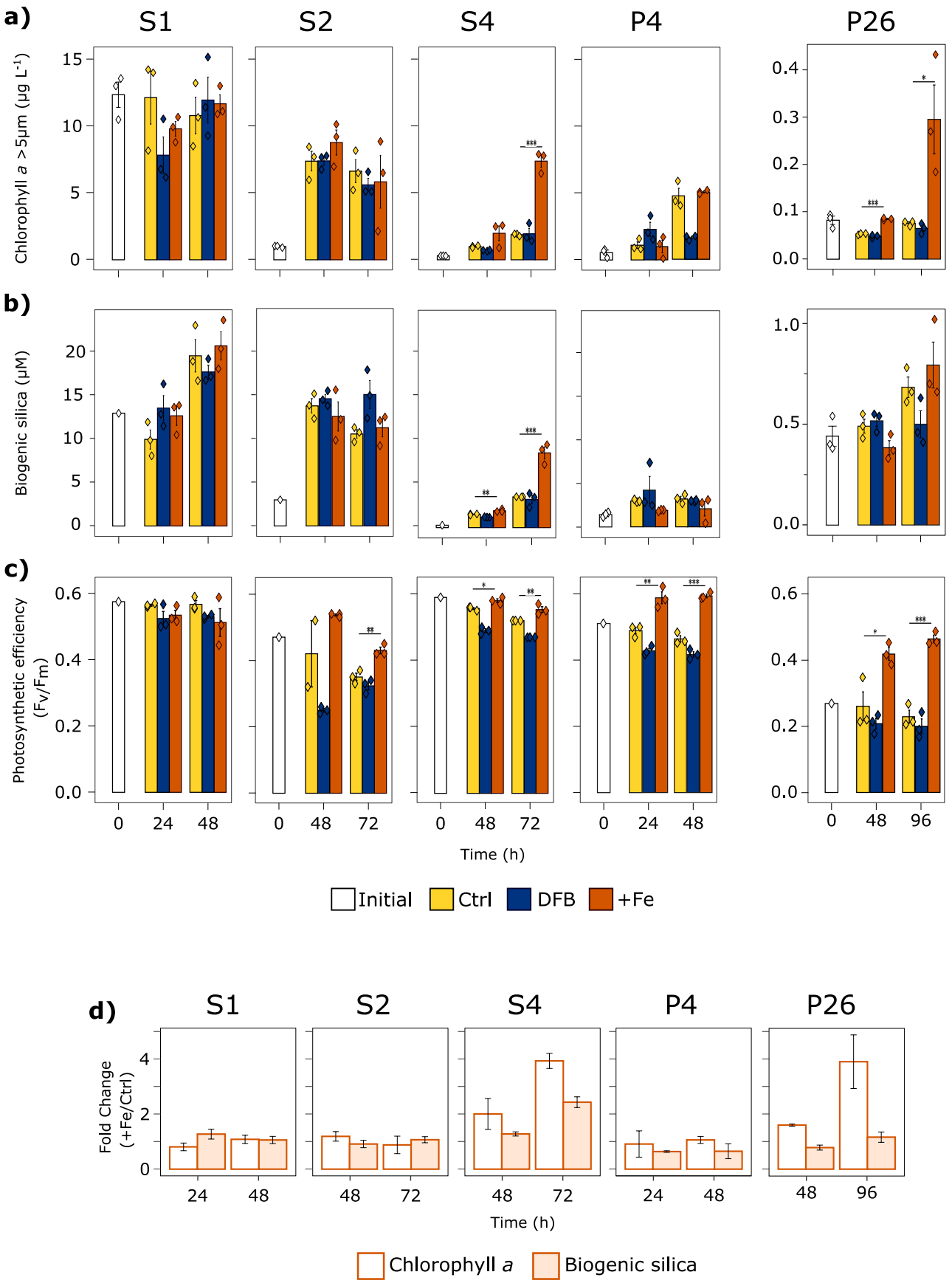


**Extended Data Fig. 1 | See next page for caption.**

**Extended Data Fig. 1 | Bulk parameters measured during incubations at each site. a,** Size-fractionated chlorophyll *a* (>5 μm; μg $L^{-1}$), **b,** biogenic silica (μM), and **c,** maximum photochemical quantum yield of photosystem II (photosynthetic efficiency; $F_v/F_m$) throughout each incubation. Treatments included an initial sample ($t_0$; open), and unamended Control (Ctrl; yellow), DFB (blue) and +Fe (orange). **d,** Fold-change in chlorophyll *a* (open bars) and biogenic silica (filled bars) between +Fe and Ctrl treatments at each timepoint. Note that at sites S2 and P4, 15 μM of $Si(OH)_4$ and 10 μM of $NO_3^-$ were added, respectively, to all treatments due to low initial concentrations ($Si(OH)_4$ at S2 < 4.7 μM; $NO_3^-$ at P4 < 1.5 μM). Mean and standard error of triplicate incubations are shown along with individual replicates (diamonds). Statistical significance of the community response to iron addition is depicted (panels **a-c**) for each time point with $^{***}P < 0.001$, $^{**}P < 0.01$, $^{*}P < 0.05$ by analysis of variance (ANOVA) followed by Tukey's HSD post hoc test. Additional statistical analysis is available in Supplementary Data 2.

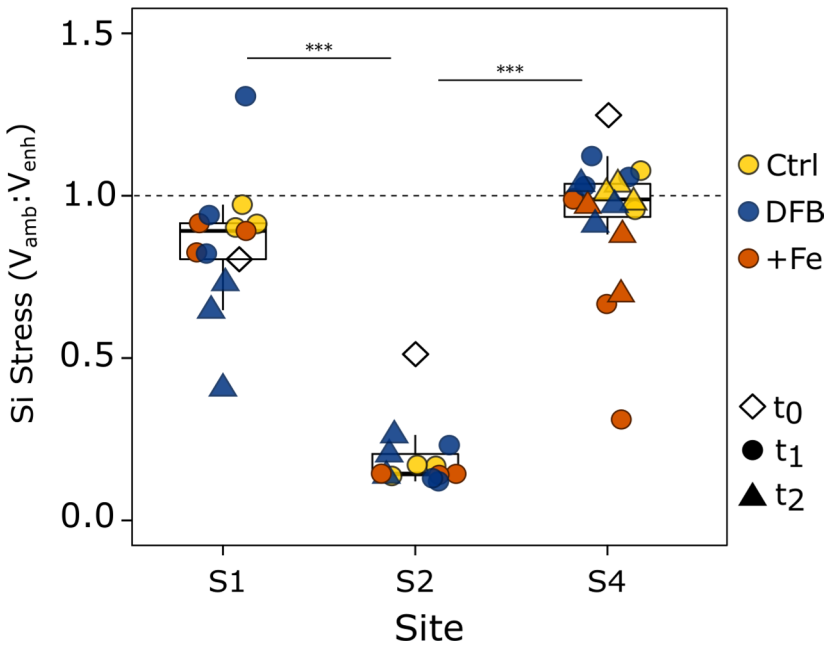


**Extended Data Fig. 2 | Silicon stress during incubation experiments at each site.** Kinetic limitation of Si uptake, or Si stress ($V_{amb}$:$V_{enh}$), at each site for initial samples ($t_0$; open diamonds) and unamended Control (Ctrl; yellow), DFB (blue) and +Fe (orange) treatments throughout each incubation experiment. Each point represents a distinct treatment (color) and time point (symbol) within each incubation (diamonds, $t_0$; circles, $t_1$, 24–48 h; triangles, $t_2$, 48–96 h). See methods and Supplementary Fig. 1 for individual time points. Values approaching zero are indicative of severe Si stress and values ~1 are indicative of silicon replete populations. The boxes depict the median (horizontal line) and upper and lower quartiles of the data with whiskers encompassing data points within 1.5× of the interquartile range. ***$P < 0.001$ by Kruskal-Wallis with Dunn's multiple comparison test. No Si stress data was collected during the P4 and P26 incubations, or at $t_2$ in the S1 and S2 incubations for Ctrl and +Fe treatments.

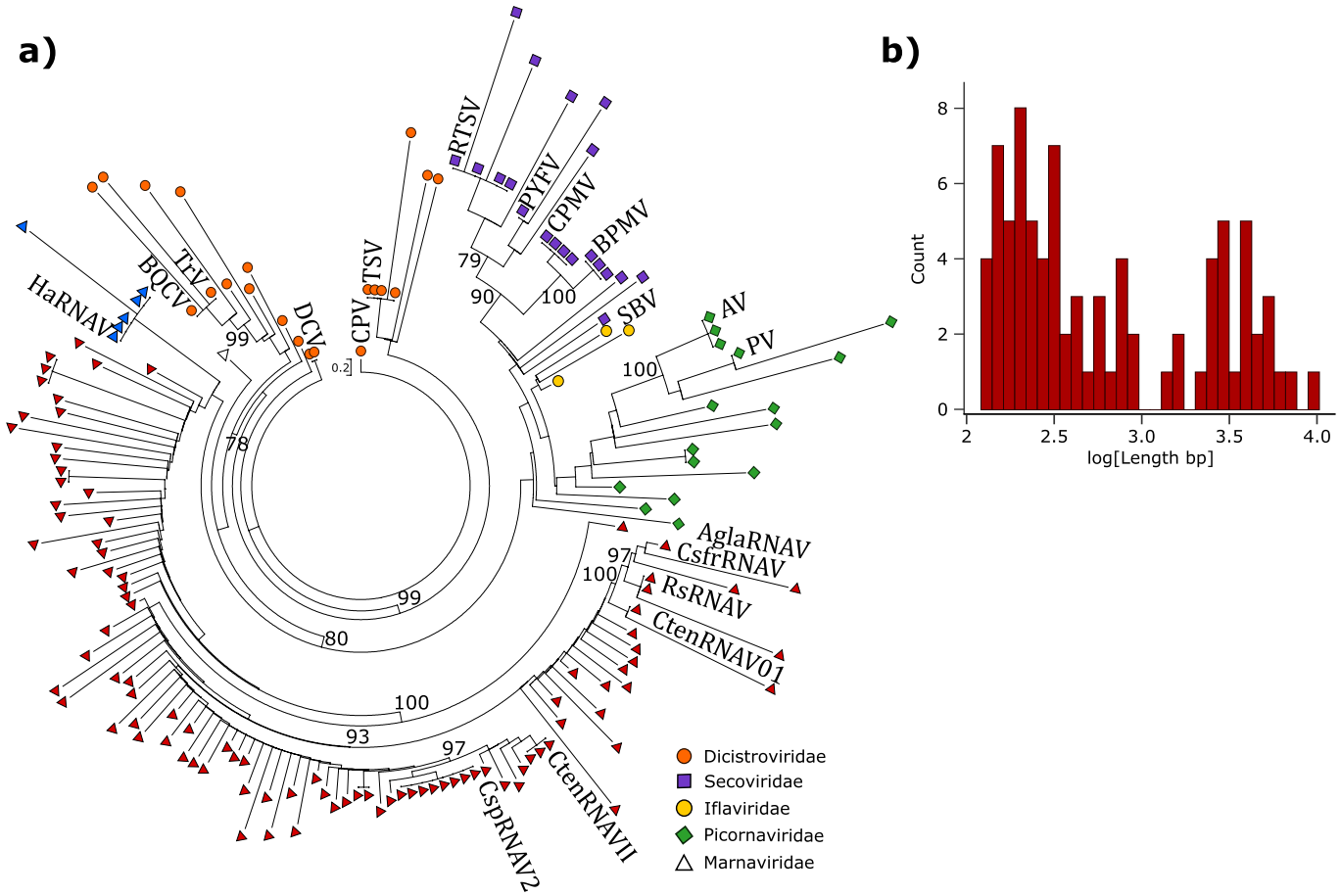


**Extended Data Fig. 3 | Phylogenetic analysis and size distribution of diatom virus-like contigs. a**, Maximum likelihood phylogenetic tree of RNA-dependent RNA polymerase (RdRp) amino acid sequences within the order *Picornavirales* and placement of homologous contigs identified in metatranscriptomes. Bootstrap values >50 are shown (100 replicates). Triangles denote sequences that fall within the family *Marnaviridae* with blue triangles denoting the genus *Marnavirus*, which is distinctly comprised of dinoflagellate viruses and red triangles identifying putative diatom viruses that were selected for downstream analysis. **b,** Size distribution (bp) of diatom virus-like contigs. The abbreviations, names and NCBI database accession numbers of the amino acid sequences used to construct the reference alignment are: AglaRNAV, *Asterionellopsis glacialis* RNA virus, BAP16719; CsfrRNAV, *Chaetoceros socialis radians* RNA virus 1, YP_002647032; RsRNAV, *Rhizosolenia setigera* RNA virus 01, YP_006732323; CtenRNAV01, *C. tenuissimus* RNA virus 01, YP_009505620; CtenRNAVII, *C. tenuissimus* RNA virus type-II, BAP99818; CspRNAV2, *Chaetoceros* species RNA virus 02, BAK40203; HaRNAV, *Heterosigma akashiwo* RNA virus, AAP97137; CPSMV, cowpea severe mosaic virus, NP_619518; BPMV, Bean pod mottle virus, NP_612349; PYFV, Parsnip yellow fleck virus, BAA03151; RTSV, Rice tungro spherical virus, NP_042507;SBV, Sacbrood virus, AIZ75645; PV, Human poliovirus 1, CAA24461; AIV, Aichi virus 1, ADN52312; BQCV, Black queen cell virus, NP_620564; TrV, Triatoma virus, NP_620562; CPV, Cricket paralysis virus, NP_647481; DCV, *Drosophila* C virus, NP_044945; TSV, Taura syndrome virus, NP_149057.

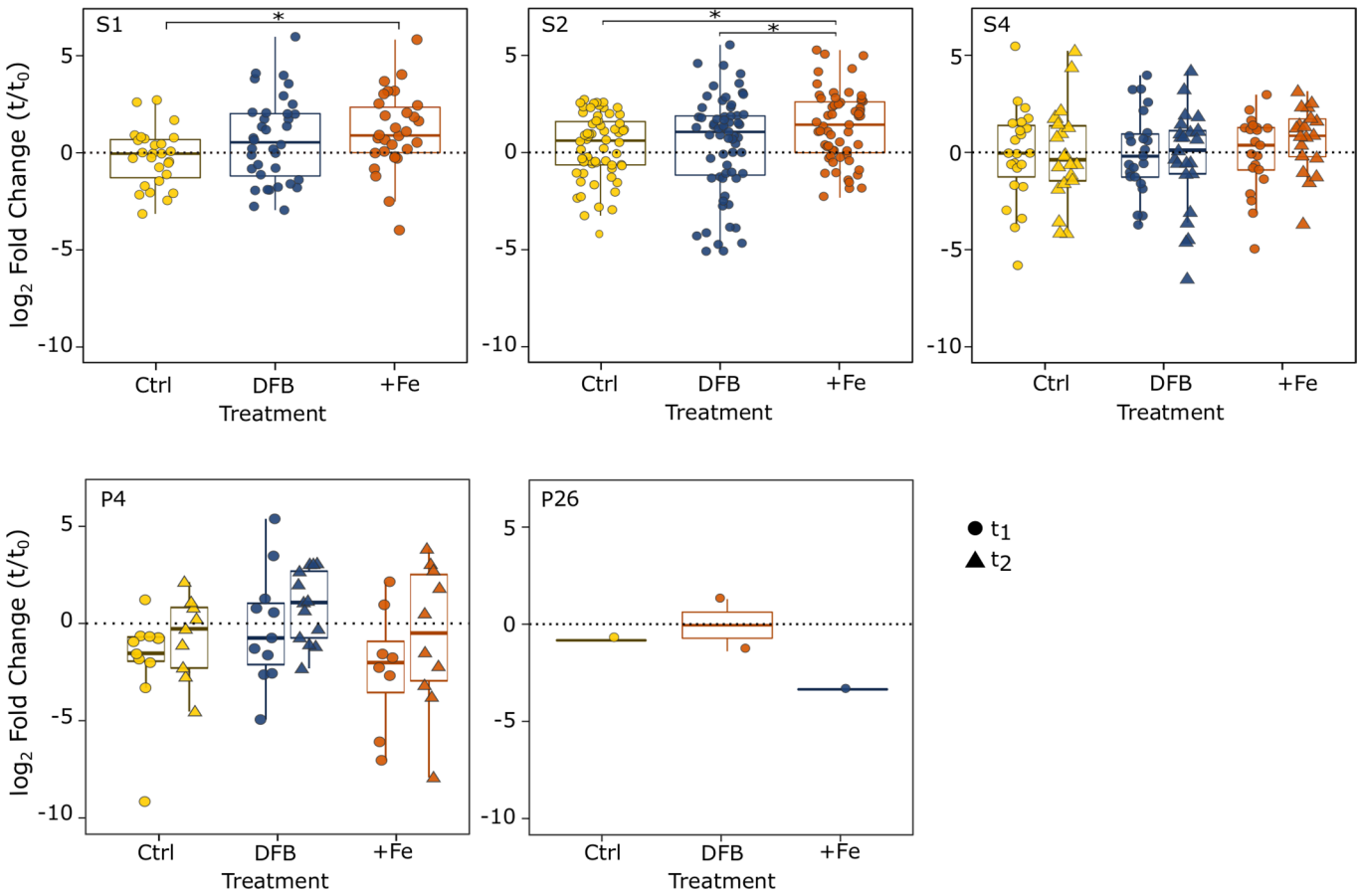


**Extended Data Fig. 4 | Temporal changes in cell-associated diatom viruses throughout each incubation.** $Log_2$ fold change in diatom virus contig abundance ($nC_v$) at $t_1$ (circles, 24–48 h) or $t_2$ (triangles, when present, 48–72 h) compared to $t_0$ for Ctrl (yellow), DFB (blue) and +Fe (orange) treatments (n = 3), $^*P < 0.05$ by a one-way analysis of variance (ANOVA) followed by a Tukey HSD post hoc test. The boxes depict the median (horizontal line) and upper and lower quartiles of the data with whiskers encompassing data points within 1.5× of the interquartile range. See methods and Supplementary Fig. 1 for individual time points (symbols) in each incubation.

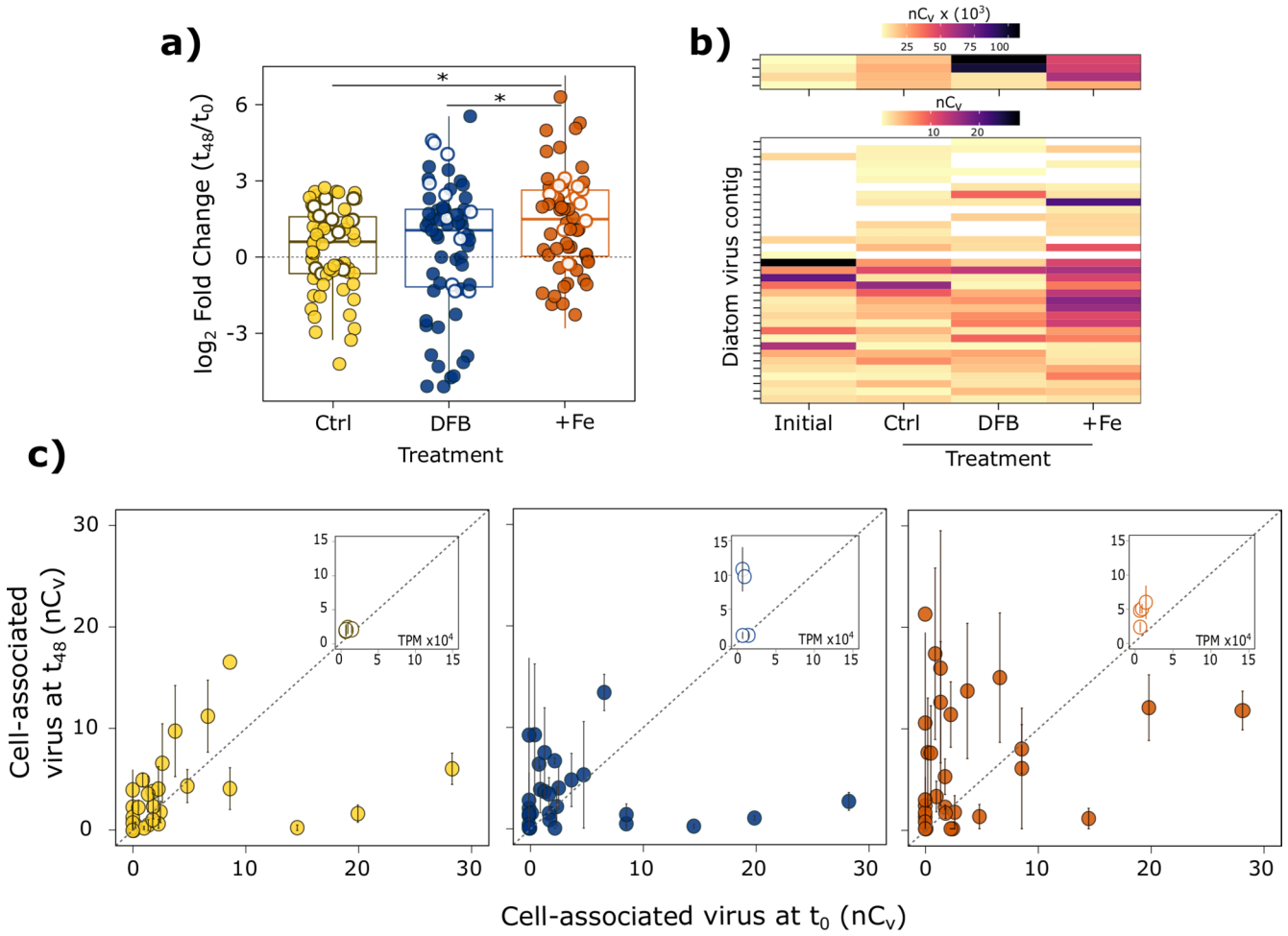


**Extended Data Fig. 5 | Temporal changes in cell-associated diatom viruses throughout the S2 incubation. a,** $Log_2$ fold change in diatom virus contig abundance ($nC_v$) between $t_{48}$ and $t_0$ for Ctrl (yellow), DFB (blue) and +Fe (orange) treatments (n = 3), $^*P < 0.05$ by a one-way analysis of variance (ANOVA) followed by a Tukey HSD post hoc test. The boxes depict the median (horizontal line) and upper and lower quartiles of the data with whiskers encompassing data points within 1.5× of the interquartile range. **b,** Heatmap of mean abundance for each diatom virus contig ($nC_v$) identified in the initial ($t_0$) sample and at $t_{48}$ across the treatments for both high (top panel) and low abundance (bottom panel) contigs. Contigs that were below detection are depicted in white. **c,** Abundance ($nC_v$) of each cell-associated diatom virus contig in Ctrl (left panel), DFB (middle panel) and +Fe (right panel) treatments at $t_{48}$ vs $t_0$. Mean ± standard error is shown (n = 3). Dotted lines denote unity-slope lines, indicating no difference between timepoints. Insets depict 'high' abundance contigs. In panels a and c, open and closed symbols denote 'high' and 'low' abundance diatom virus contigs, respectively.

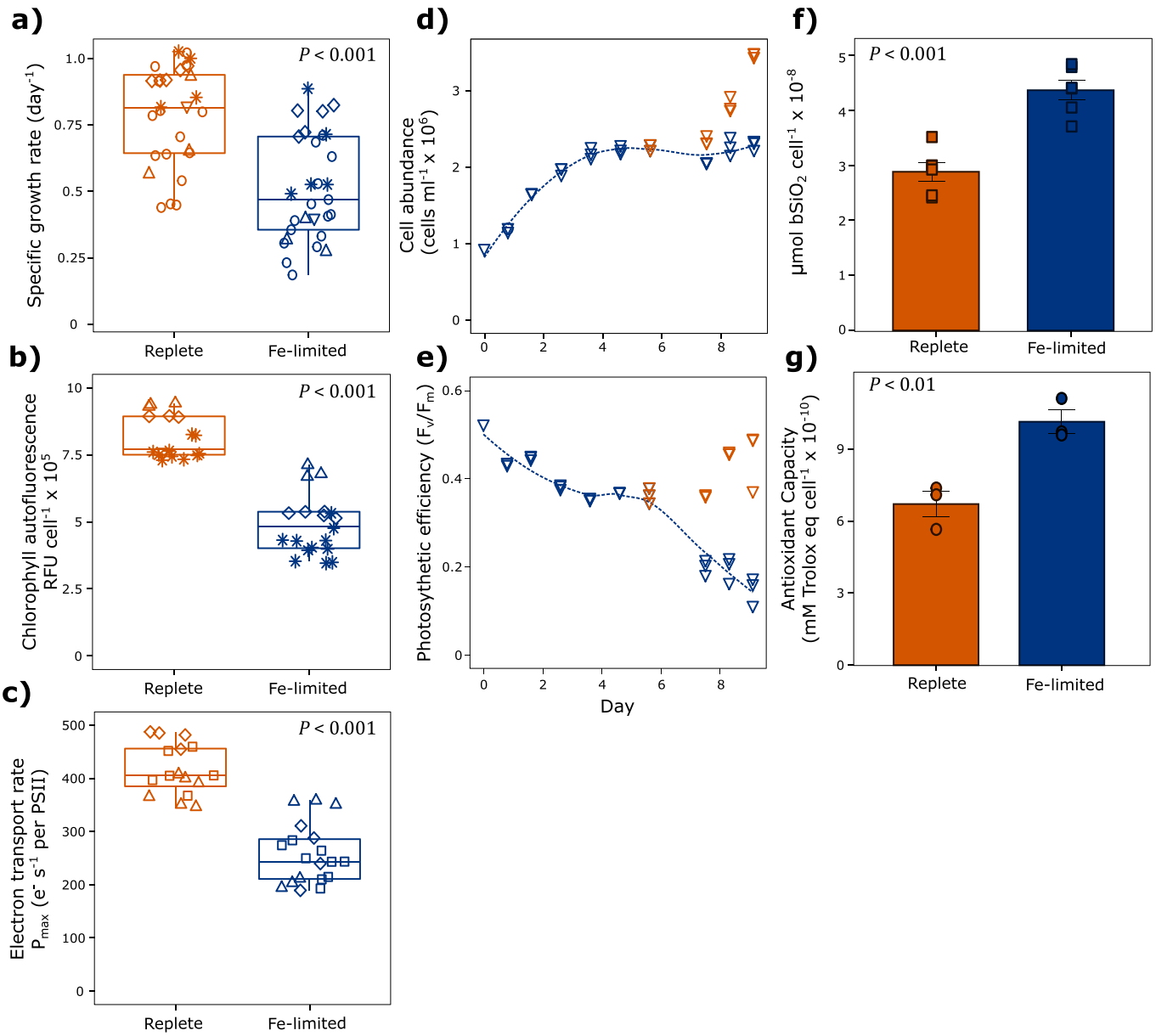


**Extended Data Fig. 6 | Diagnosing iron limitation in *Chaetoceros tenuissimus*. a,** Specific growth rates (day$^{-1}$), **b,** mean chlorophyll autofluorescence (RFU cell$^{-1}$) and **c,** electron transport rates (e$^{-}$ s$^{-1}$ PSII$^{-1}$) of C. *tenuissimus* cultures in replete (orange symbols) and Fe-limited (blue symbols) growth media. **d,** Cell abundance and **e,** maximum photochemical quantum yield of photosystem II (photosynthetic efficiency; $F_v/F_m$) during Fe-limitation (blue) and after Fe addition (orange) in an Fe 'rescue' experiment. Each independent biological replicate (n = 3) is shown by individual symbols with lines of best fit depicting a LOESS regression. **f,** cellular biogenic silica (µmol $bSiO_2$ cell$^{-1}$) and **g,** cellular antioxidant capacity (mM Trolox eq cell$^{-1}$) of replete and iron-limited *C. tenuissimus*. Statistical significance was determined using an unpaired, two-sided t-test. Different symbols denote biologically independent replicates across six independent experiments.

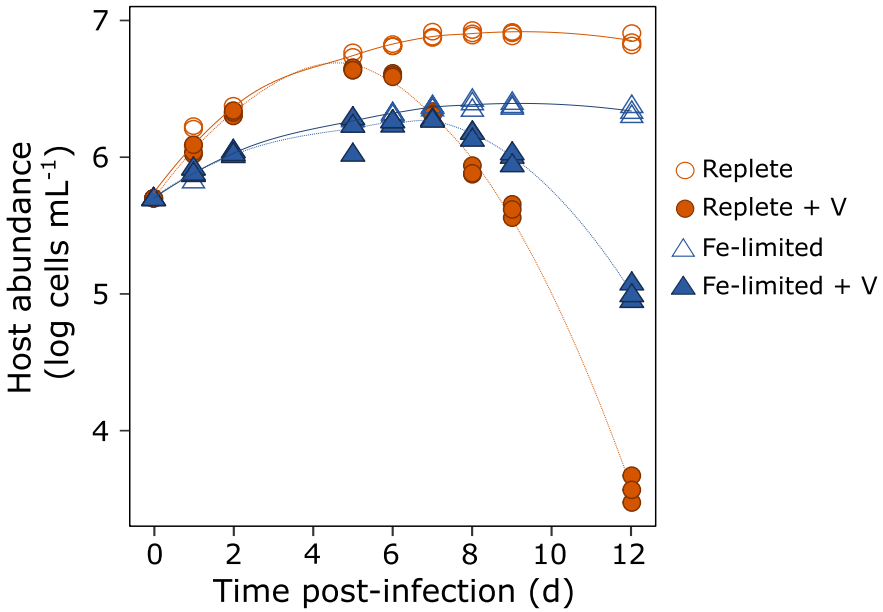


**Extended Data Fig. 7 | The impact of Fe limitation on diatom host-virus dynamics in laboratory cultures of *Chaetoceros tenuissimus* infected with CtenRNAV.** Host abundance in replete (orange circles) and Fe-limited (blue triangles), uninfected (open symbols) and infected (closed symbols) cultures with the single stranded (ss) RNA-containing virus, CtenRNAV. Individual symbols represent independent biological replicates (n = 3) with lines of best fit depicting a LOESS regression.

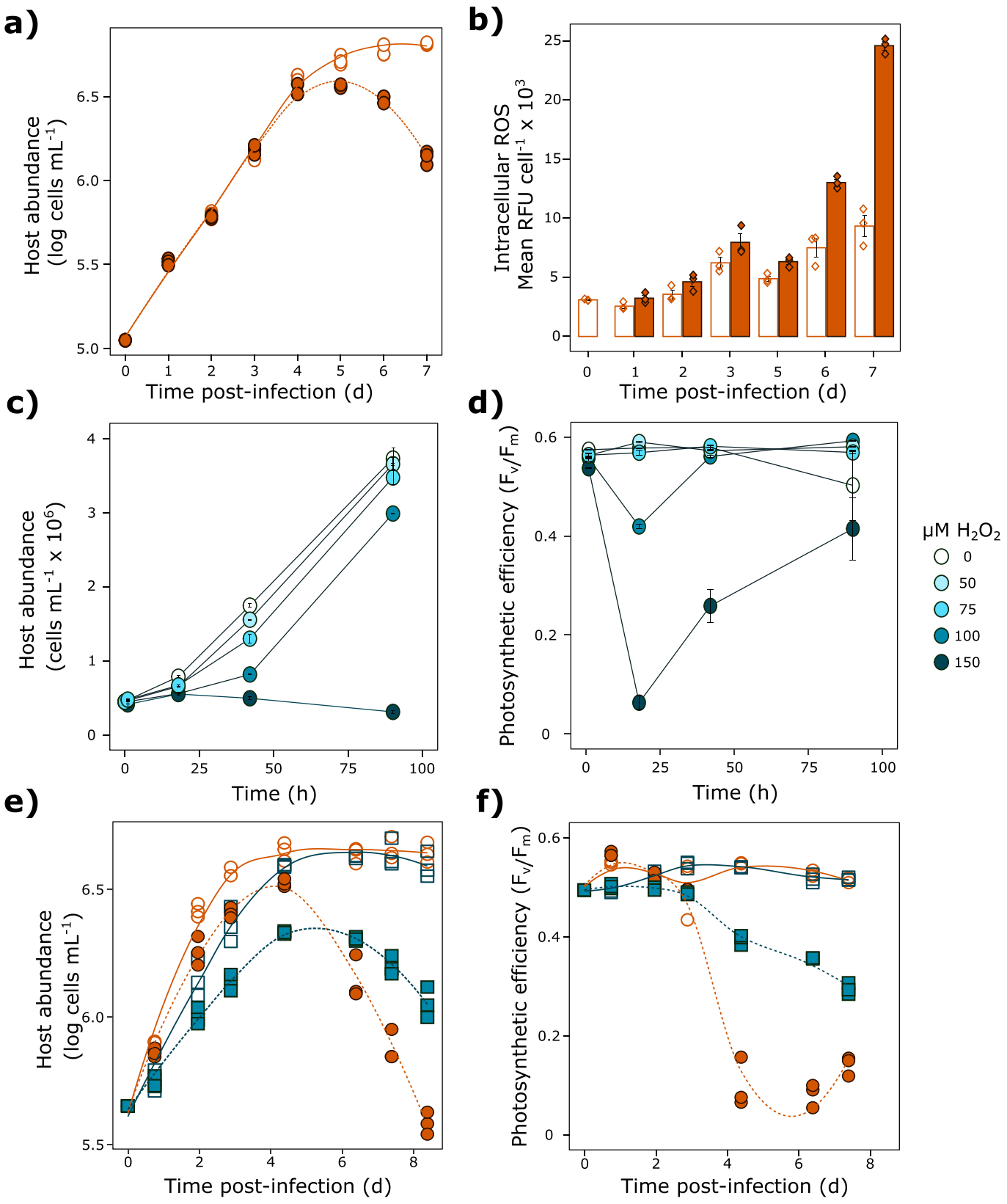


**Extended Data Fig. 8 | See next page for caption.**

**Extended Data Fig. 8 | A role for oxidative stress and reactive oxygen species during infection of *Chaetoceros tenuissimus*. a,** Host abundance and **b,** intracellular levels of reactive oxygen species (ROS; assessed by the diagnostic, fluorescent stain $H_2$DCFDA in replete, uninfected (open, orange symbols/bars) and infected (closed, orange symbols/bars) *C. tenuissimus* cultures with CtenDNAV. Mean ± standard error is shown (n = 3). **c,** Host abundance and **d,** maximum photochemical quantum yield of photosystem II (photosynthetic efficiency; $F_v/F_m$) following addition of different doses of hydrogen peroxide ($H_2O_2$; 0-150 µM). Mean ± standard error is shown for biological duplicates. Due to the observed decrease in cell abundance and photosynthetic efficiency, followed by physiological recovery, 100 µM $H_2O_2$ was chosen for downstream infection experiments. Time course of **e,** host abundance and **f,** photosynthetic efficiency during viral infection with CtenDNAV of untreated control cultures (orange circles) and cultures pre-exposed to a sub- lethal dose of $H_2O_2$ (100 µM; blue squares) for uninfected (open symbols) and infected (closed symbols) cultures (n = 3). Data are representative of three independent experiments.

**Extended Data Table 1 | Initial bulk parameters and underlying nutrient regime at each site**

| Site ID | Region | Location | Chl *a* | bSiO2 | NO3 | Si(OH)4 | Fe | Temp | Salinity | Nutrient Regime |
|---|---|---|---|---|---|---|---|---|---|---|
| S1 | CUZ | Coastal; 38°39.3N, 123°39.87W | 12.3 ± 1.63 | 12.9 | 13.7 ± 1.39 | 20.8 ± 2.53 | 3.39 | 10.7 | 33.8 | Replete |
| S2 | CUZ | Coastal; 38°15.31 N, 123°57.98W | 0.99 ± 0.07 | 2.96 | 10.3 | 4.69 ± 0.02 | 0.42 | 12.5 | 33.6 | Si-limited |
| S4 | CUZ | Coastal; 42°40N, 125°W | 0.30 ± 0.01 | 0.27 | 16.9 ± 0.22 | 19.3 ± 0.11 | 0.31 | 10.9 | 33.4 | Replete → Fe limited |
| P4 | NE Pacific | Coastal; 48°39N, 126°40W | 0.54 ± 0.34 | 1.4 ± 0.26 | 1.49 | 2.18 | 0.64 | 12.4 | 31.9 | N-limited |
| P26 | NE Pacific | Oceanic; 50°N, 145°W | 0.08 ± 0.02 | 0.44 ± 0.09 | 11.7 | 15.6 | 0.05 | 10.5 | 32.5 | Fe-limited |

Additional chemical and biological parameters measured at sites in the California Upwelling Zone (CUZ) and along the Line P transect in the subarctic northeast Pacific (NE Pacific). Site designation, region and location are included with initial measurements of chlorophyll *a* (Chl *a*; μg $L^{-1}$), biogenic Si ($bSiO_2$; μM), dissolved nitrate ($NO_3$ and $NO_2$; μM), dissolved silicic acid [$Si(OH)_4$; μM], dissolved iron (Fe; nM), temperature (Temp; °C) and salinity (PSU). Nutrient regime summarizes the underlying nutrient condition characterized for each location. When available mean and standard deviations are shown from replicate samples (n = 3).